3D hydrodynamic simulations of carbon burning in massive stars

A. Cristini,[1]★ C. Meakin,[2,3] R. Hirschi,[1,4]★ D. Arnett,[3]★ C. Georgy,[1,5]
M. Viallet[6] and I. Walkington[1]

[1]*Astrophysics Group, Keele University, Lennard-Jones Laboratories, Keele, ST5 5BG, UK*
[2]*Karagozian and Case, Inc., 700 N. Brand Blvd. Suite 700, Glendale, CA 91203, USA*
[3]*Department of Astronomy, University of Arizona, Tucson, AZ 85721, USA*
[4]*Kavli IPMU (WPI), The University of Tokyo, Kashiwa, Chiba 277-8583, Japan*
[5]*Geneva Observatory, University of Geneva, Ch. Maillettes 51, CH-1290 Versoix, Switzerland*
[6]*Max-Planck-Institut für Astrophysik, Karl Schwarzschild Strasse 1, Garching, D-85741, Germany*

ABSTRACT

We present the first detailed 3D hydrodynamic implicit large eddy simulations of turbulent convection of carbon burning in massive stars. Simulations begin with radial profiles mapped from a carbon-burning shell within a $15\,M_\odot$ 1D stellar evolution model. We consider models with 128^3, 256^3, 512^3, and 1024^3 zones. The turbulent flow properties of these carbon-burning simulations are very similar to the oxygen-burning case. We performed a mean field analysis of the kinetic energy budgets within the Reynolds-averaged Navier–Stokes framework. For the upper convective boundary region, we find that the numerical dissipation is insensitive to resolution for linear mesh resolutions above 512 grid points. For the stiffer, more stratified lower boundary, our highest resolution model still shows signs of decreasing sub-grid dissipation suggesting it is not yet numerically converged. We find that the widths of the upper and lower boundaries are roughly 30 per cent and 10 per cent of the local pressure scaleheights, respectively. The shape of the boundaries is significantly different from those used in stellar evolution models. As in past oxygen-shell-burning simulations, we observe entrainment at both boundaries in our carbon-shell-burning simulations. In the large Péclet number regime found in the advanced phases, the entrainment rate is roughly inversely proportional to the bulk Richardson number, $\mathrm{Ri_B}$ ($\propto \mathrm{Ri_B}^{-\alpha}$, $0.5 \lesssim \alpha \lesssim 1.0$). We thus suggest the use of $\mathrm{Ri_B}$ as a means to take into account the results of 3D hydrodynamics simulations in new 1D prescriptions of convective boundary mixing.

Key words: convection – hydrodynamics – turbulence – stars: evolution – stars: interiors – stars: massive.

1 INTRODUCTION

1D stellar evolution codes are currently the only way to simulate the entire lifespan of a star. This comes at the cost of having to replace complex, inherently 3D processes, such as convection, rotation, and magnetic activity, with generally simplified mean-field models. An essential question is *'how well do these 1D models represent reality?'* Answers can be found both in empirical and theoretical works. On the empirical front, we can investigate full star models, by comparing them to observations of stars under a range of conditions, as well as testing the basic physics that goes into models of multidimensional phenomena by studying relevant laboratory work and

data from meteorology and oceanography (remembering that stars are much bigger than planets, and are composed of high-energy density plasma). On the theoretical side, multidimensional simulations can be used to test 1D models under astrophysical conditions that can be recreated in terrestrial laboratories only in small volumes, e.g. in National Ignition Facility (NIF) (Kuranz et al. 2011) and z-pinch device (Miernik et al. 2013) experiments.

1.1 Astronomical tests

The results from the astronomical validation studies are mixed. Observations of stars confirm the general, *qualitative* picture of stellar evolution predicted by 1D models, but reveal significant *quantitative* differences. A recent example is the work of Georgy, Saio & Meynet (2014) and Martins & Palacios (2013) who show that the use of different criteria for convection (i.e. either Schwarzschild

★ E-mail: a.j.cristini@keele.ac.uk (AC); r.hirschi@keele.ac.uk (RH); wdarnett@gmail.com (DA)

or Ledoux) leads to important differences in the overall evolution of a massive star, especially for the post-main-sequence evolution. Without a constraint on which criteria, if either, is the correct one, this result represents an inherent uncertainty in 1D models.

These quantitative discrepancies can be reduced by modifying the treatment of convective boundaries, and more specifically, by allowing for convective penetration and overshooting (Zahn 1991). Incorporating a model for mixing beyond the linearly stable convective boundaries (e.g. that given by the Ledoux or Schwarzschild criteria) introduces additional parameters that can be tuned to improve agreement between model and data (Freytag, Ludwig & Steffen 1996). However, this approach has several drawbacks beyond the obvious one of overfitting so as to preclude a predictive model. Perhaps the most egregious is that parameter fitting is never done in a global sense so that different phases of evolution require different parameters, thus revealing the non-universality of these models. Another recent example is the finding that stellar models of red giants agree with Kepler observations only when a metallicity-dependent mixing length is used (Tayar et al. 2017).

1.2 Computational methods and assumptions

The most obvious way to proceed computationally is by direct numerical simulation (DNS), in which all relevant scales of the turbulent cascade are resolved. This is not feasible with present or foreseeable computer power. The Reynolds numbers for stars are enormous (e.g. Re $\approx 10^{18}$, Arnett, Meakin & Viallet 2014), simply because stellar dimensions are so much larger than mean-free paths for dissipation. DNS requires an infeasible dynamic range in order to include both the microscopic and macroscopic scales; for example the state-of-the-art DNS work of Jonker et al. (2013) attained a Reynolds number of 10^3 with a Péclet number of unity.

An alternative is possible. The largest eddies contain most of the energy in a turbulent cascade. Kolmogorov's second similarity hypothesis, which posits that the rate of dissipation in a turbulent flow as well as the statistics in the inertial sub-range do not depend upon the detailed nature of the dissipative process, implies that it may be unnecessary to resolve the dissipation sub-range to accurately calculate scales above the Kolmogorov scale, provided that the behaviour of the sub-grid dissipation is well behaved. This phenomenology has indeed been supported by detailed numerical studies (see Aspden et al. 2008). Even early implicit large eddy simulations (ILES) with relatively coarse resolution (Meakin & Arnett 2007b) gave Kolmogorov dissipation at the sub-grid scale; this is because they use a finite volume and total variations diminishing solver (piecewise parabolic method, PPM; see Colella & Woodward 1984), ensuring that mass, momentum, and energy are conserved and variance is dissipated at the grid scale.

Comparative studies of using DNS to solve the compressible Navier–Stokes equations and ILES to solve the inviscid Euler equations using PPM have been performed (Porter & Woodward 2000; Sytine et al. 2000). Comparisons were made on grids with sizes from 64^3 to 1024^3. Both methods were found to converge to the same limit with increasing resolution. A factor in deciding whether DNS or ILES is a more suitable choice depends on whether the phenomena of interest require resolution of the dissipative range or not. We currently do not have a compelling argument for resolving the dissipation range in the current work.

Furthermore, the additional information provided explicitly by DNS, such as dissipation rates, can often be estimated very accu-

rately when the ILES method is used in conjunction with Reynolds-averaged Navier–Stokes (RANS) methods; at least in the mean. This is a point we discuss in Section 4.4 below and in Viallet et al. (2013), Arnett et al. (2015), and Arnett & Meakin (2016).

1.3 Stellar simulations

ILES simulations sampling a broad range of relevant and increasingly more realistic astrophysics conditions have been undertaken. Neutrino cooling becomes dominant after helium burning, so that later stages have increasingly shorter thermal time-scales (see Arnett 1996, pp. 284–292), which are insensitive to radiative diffusion or heat conduction (high Péclet number,[1] Pe $\gg 1$). Oxygen burning has both a relatively simple nuclear-burning process, and a short thermal time, so that a small but significant fraction of the burning stage may be simulated (Meakin & Arnett 2007b), with a Damköhler number,[2] Da, approaching 1 per cent (see Table A1 for estimates of Da for various burning stages).

Many oxygen-burning simulations have been performed, giving an improved understanding of the process; e.g. Arnett (1994), Bazan & Arnett (1994), Bazán & Arnett (1998), Asida & Arnett (2000), Kuhlen, Woosley & Glatzmaier (2003), Young et al. (2005), Meakin & Arnett (2006), Meakin & Arnett (2007a), Meakin & Arnett (2007b), Arnett & Meakin (2011a), Viallet et al. (2013), Arnett et al. (2015), Arnett & Meakin (2016), and Jones et al. (2017).

Silicon burning is the most complex burning phase, complicated by active nuclear weak interactions, and requires a large additional computational effort. The evolution time-scale is of the order of days (Da ~ 1 and Pe $\gg 1$). Early simulations of silicon burning (Bazán & Arnett 1997) used a nuclear reaction network consisting of 123 nuclei. Meakin (2006) and Arnett & Meakin (2011a) performed 2D simulations of concentric carbon-, oxygen-, and silicon-burning shells using a 37 species network for several convective turnovers about one hour prior to core collapse. Couch et al. (2015) simulate the final three minutes of silicon burning in a $15\,M_\odot$ star, using the FLASH code (Fryxell et al. 2000) with adaptive mesh refinement, and a nuclear reaction network of 21 species. An initial study of silicon burning with a large network ($\sim$120 nuclei) has been carried out by Meakin & Arnett (in preparation). The carbon, oxygen, and part of the silicon shell of an $18\,M_\odot$, unrelaxed spherical star have also been simulated, in a full-sphere simulation with low resolution ($400 \times 148 \times 56$) by Müller et al. (2016).

Early phases of stellar evolution are harder to simulate because they are generally characterized by very small Damköhler numbers (slow burning) and very low convective Mach numbers (slow mixing). Several studies have targeted hydrogen- or helium-burning phases. Meakin & Arnett (2007b) performed a fully compressible simulation of core hydrogen burning on a numerical grid of 400×100^2, with the driving luminosity boosted by a factor of 10. Gilet et al. (2013) adopt the low Mach number solver MAESTRO (Almgren, Bell & Zingale 2007) to simulate core hydrogen burning on a numerical grid of 512^3. This type of solver removes the need

---

[1] The Péclet number is the ratio of the time-scale for transport of heat through conduction to the time-scale for transport of heat through advection, or Pe $= vL/\chi$, where v and L are the characteristic velocity and length-scale of the flow and χ is the heat diffusivity (e.g. Lautrup 2011, p. 380).

[2] The Damköhler number is the ratio of the advective time-scale to the chemical/nuclear time-scale (Damköhler 1940), or Da $= \tau_c /(qX_i/\epsilon_{nuc})$, where τ_c is the convective turnover time and ϵ_{nuc}, q, and X_i are the energy generation rate, specific energy released, and abundance fraction for the dominant nuclear reaction, respectively.

to follow the propagation of acoustic waves, and allows for longer time-steps than a fully compressible solver, but would neglect any important kinetic energy transfer due to acoustic fluxes.

We have performed novel calculations of a yet to be simulated phase of evolution, the carbon phase in a massive star, which we studied in a burning shell within a 15 $M_\odot$ massive star. Carbon burning is the first neutrino-cooled-burning stage, thus allowing radiative diffusion to be neglected (Pe $\gg$ 1) and slightly simplifying the numerical model. It is characterized by a larger Damköhler number than earlier, radiatively cooled stages, alleviating the computational cost. The initial composition and structure profiles are simpler than those of more advanced stages, because the region in which the shell forms is smoothed by the preceding convective helium-burning core. Finally, as the first neutrino dominated phase of nuclear burning it plays an important role is setting the size of the heavy element core which subsequently forms and in which a potential core-collapse event may take place. We are particularly interested in the structure of convective boundaries and composition gradients, in this sense we explore the effects of resolution (zoning) upon the simulations. Composition is treated as an active scalar, and coupled to the fluid flow through advection and the equation of state (EOS).

The structure of the paper is as follows. In Section 2, we discuss the stellar model from which the initial conditions for our hydrodynamic models were selected. In Section 3, we describe our simulation model set-up. Our results and analysis of the hydrodynamic models are presented in Section 4. We compare our models to similar simulations in Section 5. Finally, in Section 6, we summarize our results.

2 INITIAL CONDITIONS

2.1 The 1D stellar evolution model

To prepare the input for the 3D carbon-burning simulations, we calculated a 15 $M_\odot$, solar metallicity, non-rotating model until the end of the oxygen-burning phase using the Geneva stellar evolution code (GENEC; Eggenberger et al. 2008). The default input physics used in GENEC to calculate this model includes: a nuclear reaction network of 23 isotopes using the Nuclear Astrophysics Compilation of Reaction Rates (NACRE) (Angulo et al. 1999) tabulated reaction rates; EOS describing a perfect gas, partial degeneracy, and radiation; opacity tables from the OPAL group (Rogers, Swenson & Iglesias 1996) and Alexander & Ferguson (1994) for high and low temperatures, respectively; mass loss estimated according to the prescriptions by Vink, de Koter & Lamers (2001) and de Jager, Nieuwenhuijzen & van der Hucht (1988); concentration and thermal diffusion; convection treatment using mixing length theory (MLT) with $\alpha_{ml} = 1.6$ (Schaller et al. 1992); convective boundary positions determined using the Schwarzschild criterion (Schwarzschild & Voigt 1992); and penetrative convective overshoot (Zahn 1991) up to 20 per cent (Stothers & Chin 1991) of the pressure scaleheight for core hydrogen and helium burning only.

Fig. 1 presents the evolution of the convective structure of this 15 $M_\odot$ model. Convectively unstable regions are indicated in this figure by shaded areas with colour indicating the convective Mach number, which slowly rises as the star evolves, being lowest in the core and highest in the envelope.

2.2 An overview of stellar convection parameters

In order to place the results of our carbon shell simulations into the broader context of stellar convection over the lifetime of the star, as
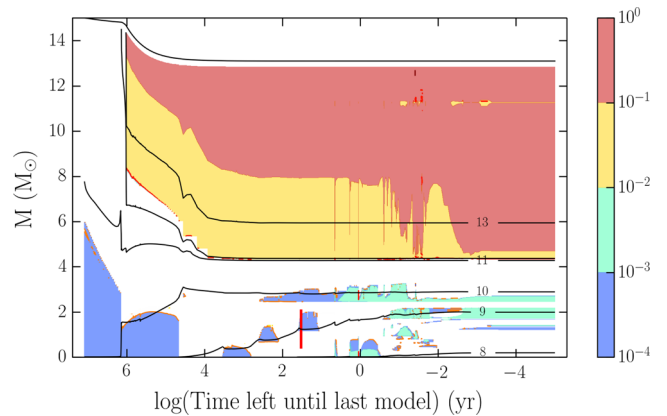

Figure 1. Structure evolution diagram of the 15 $M_\odot$ 1D input stellar model. The horizontal axis is a logarithmic scale of the time left before the predicted collapse of the star in years (the last model in this simulation is before the end of silicon burning, but since the time-scale of silicon burning is so short this does not affect the plot for the earlier phases) and the vertical axis is the mass in solar masses. The total mass and radial contours (in the form $\log_{10}(r)$ in cm), are drawn as solid black lines. Shaded areas correspond to convective regions. The colour indicates the value of the Mach number. The red vertical bar around $\log[$time left in years$]$ $\sim$1.5 represents the domain simulated in 3D, and the time at which the 3D simulations start, relative to the evolution of the star.

well as inform the construction of initial states for future simulations, we have estimated key quantities for most of the convective zones in the 15 $M_\odot$ model (Fig. 1). These quantities include the bulk Richardson number, Ri_B (equation A5); convective velocity, v_c (equation A6); Mach number, Ma (equation A7); Péclet number, Pe (equation A8); and Damköhler number, Da (equation A10). These values and the methods by which they have been calculated are presented in Appendix A. These are order of magnitude estimates intended to show trends between different stages of evolution.

One additional key property of the advanced convective regions in massive stars is the radial extent (see the radial contours in Fig. 1). For the mass range that we consider, such convective regions typically span only a few pressure scaleheights (0.2–5), convection, in this case, is classified as shallow.[3] Consequently, convective motions might be expected to resemble at least some characteristics of the classical description of convective rolls proposed by Lorenz (1963), a hypothesis that shows some validity according to the results of Arnett & Meakin (2011b).

Referring to Table A1, the 1D model (shown in Fig. 1) shows a general increase in the convective velocities and the Mach, Péclet, and Damköhler numbers as the star evolves. Some additional trends of interest include the following.

Convective velocity. The convective velocities range from about 5×10^4 cm s^{-1} during the early phases to a few times 10^6 cm s^{-1} during the advanced phases.

Mach number. The Mach number ranges from a few times 10^{-4} (values lowest for helium and carbon burning) to close to 10^{-2} (several times 10^{-2} for 3D simulations). Note that the Mach number may still increase further during silicon burning and the early collapse as found by Arnett (1996) and Müller et al. (2016).

Péclet number. The Péclet number is always much larger than one, with a minimum around 1000 during hydrogen burning and up

---

[3] An example of deep convection is in the envelopes of red giants, which extends over many pressure scaleheights.

to 10^{10} during the advanced phases. Radiative effects may still dominate at smaller scales as discussed in Viallet et al. (2015) and they certainly play an important role during the early stages of stellar evolution. As mentioned in Section 1, for most of the convective phases, the evolutionary time-scale is much larger than the advective time-scale (Da $\sim 10^{-7}$ for hydrogen burning). Only during the later stages of evolution do these time-scales become comparable (Table A1; Da $> 10^{-4}$).

For carbon and oxygen burning, Pe $\gg 10^6$. This is a consequence of neutrino cooling, which shortens the thermal time-scale but does not affect the radiative/conductive cooling rate. The specific entropy, S, obeys

$$\mathrm{d}S/\mathrm{d}t = \partial S/\partial t + (1/\rho)\nabla\cdot\boldsymbol{v}\rho S = \epsilon/T - (1/\rho T)\nabla\cdot\boldsymbol{F}_{rad}, \quad (1)$$

where ρ, $\boldsymbol{v}$, T, and $\boldsymbol{F}_{\mathbf{rad}}$ are the density, flow velocity, temperature, and radiative flux, respectively. $\epsilon = \epsilon_{\mathrm{nuc}} + \epsilon_\nu$ is the net heating from nuclear burning and neutrino cooling. If $\epsilon = 0$, Rayleigh's criterion for convection may be derived (Turner 1973). If $\boldsymbol{F}_{rad} = 0$ then the condition for simmering convection during a thermal runaway may be found (Arnett 1968).

Bulk Richardson number. Another important result relates to the bulk Richardson number which is a measure of the stiffness of the convective boundary, as well as of the boundary mixing rate. A key factor in $\mathrm{Ri_B}$ is the buoyancy jump at the boundary (equation A4) which has contributions from both entropy and mean molecular weight (μ) gradients. At the start of burning, the thermal component of the entropy gradient dominates. However, as nuclear burning proceeds, the μ gradient increases and starts to dominate over the thermal component. Even during the hydrogen-burning phase where the convective core continuously recedes, the μ gradient ultimately dominates over the thermal component.

The Richardson number[4] measures the ratio of potential energy from stable stratification to the turbulent kinetic energy (TKE) at the boundary, and so provides an asymptote for entrainment solutions; mixing is limited by the energy available. The actual rate of entrainment depends also upon the effectiveness with which that energy is deposited in the stable layer rather than being advected back into the convective region (which may be related to the Péclet number). DNS simulations (e.g. Jonker et al. 2013) typically use Pe ~ 1, appropriate for air and not far from Pe ~ 7 which may be more appropriate for water. Experiments usually have comparable Péclet numbers.

During the advanced burning stages (C, Ne, O, and Si burning), the convective core grows during most of the stage and the boundary becomes 'stiffer' as μ gradients increase. As the end of the burning stage is approached, the convective regions recede and the boundary stiffness decreases as the μ gradient is weakened.

We compared the bulk Richardson number between different phases and found in general that the boundary was at its 'stiffest' during the maximum mass extent of the convective regions, and 'softest' at the very end of each burning stage. The values we estimated for $\mathrm{Ri_B}$ for core carbon and oxygen burning (see Table A1) agree well with the trend described above. The evolution of $\mathrm{Ri_B}$ for the other core-burning stages, however, does not necessarily follow the same trend. This is partly due to the fact that it is not straightforward to estimate $\mathrm{Ri_B}$ from a 1D model. In particular, it is

---

[4] Here, we use the bulk Richardson number to denote a global measure of the stiffness of boundaries, but do not preclude the possibility that other varieties of Richardson number may eventually prove advantageous (e.g. Arnett et al. 2015).
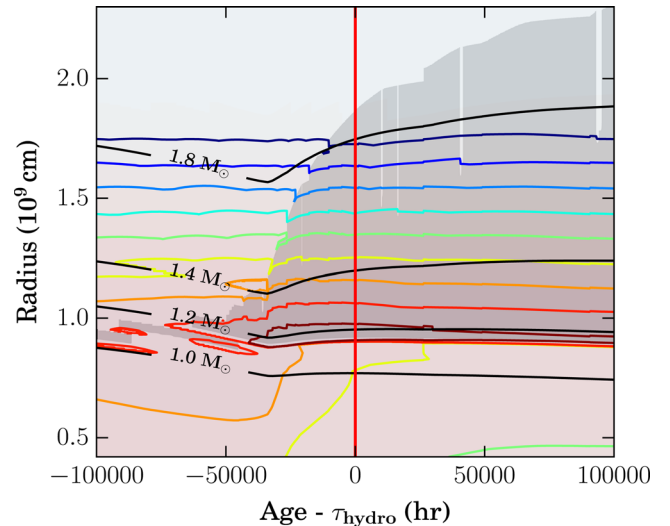

Figure 2. Convective structure evolution diagram of the $15\,\mathrm{M}_\odot$ stellar model used as initial conditions in a 3D hydrodynamics simulation friendly format. The horizontal axis is the time relative to the start of the 3D simulations (τ_{hydro}). The vertical axis is the radius in 10^9 cm. Mass contours in solar masses are shown by black lines and nuclear energy generation rate contours by coloured lines, dark red corresponds to $10^9\,\mathrm{erg\,g^{-1}\,s^{-1}}$, and the remaining colours decrease by one order of magnitude. Blue and pink shading represent regions of negative and positive net energy generation, respectively. Grey-shaded areas correspond to convective regions. The vertical red bar indicates the start time and radial extent of the hydrodynamical 3D simulation. The physical time of the simulation is on the order of 1 h, still much shorter than the time-scale of this plot.

not easy to define the integration length, Δr to be used in calculating the buoyancy jump defined in equation (A4) (see Cristini et al. 2016, for additional details).

$\mathrm{Ri_B}$, and thus the character of stellar convective boundaries, can be expected to vary significantly during the course of stellar evolution. Therefore, developing a convective boundary mixing model that incorporates this information would be a major advancement over most of the models currently in use.

Finally, the lower boundary of the convective shells are consistently found to be stiffer than the upper boundary. This has important implications for astrophysical phenomena that involve convective boundary mixing (CBM) at the lower boundaries of convective shells. For example, the onset of novae (Denissenkov et al. 2013a), and flame front propagation in S-asymptotic giant branch stars (Denissenkov et al. 2013b) which can change the model from being an electron-capture supernova progenitor to a core-collapse supernova progenitor (Jones et al. 2013).

2.3 Initial model for 3D hydrodynamic simulations

We focus in this study on the second carbon-burning shell of the $15\,\mathrm{M}_\odot$ star shown in Fig. 1. Choosing the carbon shell as opposed to the core allows us to study two physically distinct boundaries rather than one.

Fig. 2 presents a Kippenhahn diagram for the carbon shell region. The vertical red bar in this figure shows the time at which the simulations start as well as the vertical extent of the computational domain used. The horizontal axis shows the age of the star relative to its age at the start of the 3D hydrodynamic simulations. We can see in Fig. 2 that the 3D simulations correspond to the initial phase of the carbon-burning shell, during which the convective shell grows

in mass in the 1D model. The physical time of the 3D simulations, however, is on the order of hours, much shorter than the time-scale on the horizontal axis. Furthermore, the bottom of the convective shell is stable (horizontal mass contour for 1.2 M$_\odot$). Thus, we do not expect strong structural re-arrangements (not considered in the 3D simulations as we are using a constant gravity, see Section 3.3) to occur over the time-scale of the 3D simulations. The mass extent of the computational domain is 0.4 M$_\odot$ < M < 2.1 M$_\odot$ and as can be seen in Fig. 2, the domain contains a stable radiative zone on both sides of the convective shell.

3 3D HYDRODYNAMIC SIMULATIONS

3.1 The physical model

We compute 3D hydrodynamic simulations using the PROMPI code (Meakin & Arnett 2007b). PROMPI is a finite-volume, Eulerian code derived from the legacy astrophysics code PROMETHEUS (Fryxell, Müller & Arnett 1989), which uses the PPM of Colella & Woodward (1984). PROMPI is parrallelized using the message passing interface (MPI). The base hydrodynamics solver can be complemented by several microphysics prescriptions: the Helmholtz EOS of Timmes & Swesty (2000); an arbitrary nuclear reaction network; self-gravity in the Cowling approximation (e.g. pg. 86 of Prialnik 2000) relevant for deep interiors; multispecies advection; and radiative diffusion (although neglected in these simulations).

PROMPI solves the Euler equations (inviscid approximation), given by:

$$\frac{\partial \rho}{\partial t} + \nabla \cdot (\rho \, \boldsymbol{v}) = 0; \tag{2}$$

$$\rho \, \frac{\partial \boldsymbol{v}}{\partial t} + \rho \, \boldsymbol{v} \cdot \nabla \boldsymbol{v} = -\nabla p + \rho \, \mathbf{g}; \tag{3}$$

$$\rho \, \frac{\partial E_{\mathrm{t}}}{\partial t} + \rho \, \boldsymbol{v} \cdot \nabla E_{\mathrm{t}} + \nabla \cdot (p \, \boldsymbol{v}) = \rho \, \boldsymbol{v} \cdot \mathbf{g} + \rho(\epsilon_{\mathrm{nuc}} + \epsilon_{\nu}); \tag{4}$$

$$\rho \, \frac{\partial X_{\mathrm{i}}}{\partial t} + \rho \, \boldsymbol{v} \cdot \nabla X_{\mathrm{i}} = R_{\mathrm{i}}, \tag{5}$$

where p is the pressure, $\mathbf{g}$ the gravitational acceleration, E_{t} the total energy, X_{i} the mass fraction of nuclear species i, and R_{i} the rate of change of nuclear species i.

While there is evidence that magnetic fields will be generated in deep interior convection (e.g. Boldyrev & Cattaneo 2004) and that rotational instabilities (e.g. Maeder et al. 2013) may play an important role in shaping convection, we focus purely on the hydrodynamic aspects in the current study, which remains a problem of significant complexity with many outstanding issues.

Energy generation during carbon burning proceeds mainly via fusion of two ^{12}C nuclei. For stellar conditions, considering only the main exit channels (α and p) will result in no significant errors (Arnett 1996). The n exit channel branching ratio is only $b_n = 0.02$, so for this study we only consider energy generation due to the α and p channels. We estimated the carbon-burning energy generation rate in our 3D simulations with a slightly modified version of the parametrization given by Audouze, Chiosi & Woosley (1986) and Maeder (2009):

$$\epsilon_{^{12}\mathrm{C}} \sim 4.8 \times 10^{18} \, Y_{12}^2 \, \rho \, \lambda_{12,12}, \tag{6}$$

where $Y_{12} = X_{^{12}\mathrm{C}}/12$, $\lambda_{12,12} = 5.2 \times 10^{-11} \, T_9{}^{30}$, and $T_9 = T/10^9$.

This simplification to the nuclear physics allows us to represent the stellar material using only three compositional quantities: the

average atomic mass $\bar{A}$, average atomic number $\bar{Z}$, and the carbon abundance $X_{^{12}\mathrm{C}}$. The mass and charge are required for the EOS and to represent the mean properties of all other species besides ^{12}C. Thus, the composition is an active scalar, and coupled to the flow through the EOS and mixing. A further simplification is that the change of ^{12}C due to nuclear burning was ignored because of its negligible rate of change relative to advective mixing over such short time-scales (i. e. the carbon shell is characterized by a very small Damköhler number, Da $\sim 10^{-4}$, see Table A1). The key important feature retained with this prescription of the nuclear burning is the interaction and feedback between the nuclear burning and hydrodynamic mixing, while keeping computational costs to a minimum.

Cooling via neutrino losses is parametrized using the analytical formula provided by Beaudet, Petrosian & Salpeter (1967) which includes all of the relevant processes: pair creation reactions, Compton scattering, and plasma neutrino reactions. The cooling is essentially constant over the simulation time and its details are not important for our purposes.

3.2 The computational domain

Approximations are necessary to simulate a meaningful physical time. In this study, we follow the 'box-in-star' approach (Arnett & Meakin 2016) and we use a Cartesian coordinate system and a plane-parallel geometry. We evolve the model with time-steps determined by the Courant condition, using a Courant factor of 0.8. Our computational domain represents a convective region of thickness, t, bounded either side by radiative regions of thickness, $t/2$. The aspect ratio of the convective zone is therefore 2:1 (width:height), and so a plane-parallel approximation is not ideal and is the first major simplification of our set-up. We made this choice to allow us to ease the difficult Courant time-scale condition at the inner boundary of the grid allowing for longer run-times, as well as better resolution near convective boundaries. Direct comparison with the oxygen-burning simulations, which use a spherical grid, suggest that no significant error results.

In order to study the complete convective region, and also stable region dynamics (such as wave propagation), we chose to include the entire convection zone and portions of the adjacent stable regions. The radial extent of the domain in relation to the stellar model initial conditions is illustrated in Fig. 2 by the vertical red bar. The computational domain extends in the vertical (x) direction from 0.42×10^9 cm to 2.30×10^9 cm, and in the two horizontal directions (y and z) from 0 to 1.88×10^9 cm, see Fig. 3.

We found that the aspect ratio for the convective zone of 2:1 was the required minimum for unrestricted circulation of turbulent fluid elements. The radial extent of the computational domain represents 4×10^{-5} of the total radius of the star, which is 4.6×10^{13} cm. At the chosen evolutionary stage, the shell is expanding, as can be seen in Fig. 2, and the luminosity is driven by a peak in nuclear energy generation of $\sim 10^9$ erg g^{-1} s^{-1} at $x \sim 0.9 \times 10^9$ cm.

The computational domain uses reflective boundary conditions in the vertical direction and periodic boundary conditions in the two horizontal directions. Although the material in the radiative regions is stable against convection, it has oscillatory g-mode motions excited by the adjacent convection zone. In order to mimic the propagation of these waves out of the domain, we employ a damping region that extends radially between a radius of 0.6×10^9 cm and the lower domain boundary at 0.42×10^9 cm. The damping region covers the full horizontal extent of the computational domain in between these radii. Within this region, all velocity components
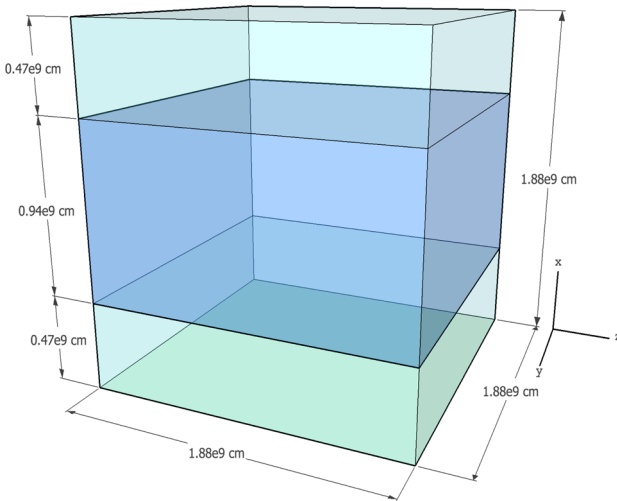
Figure 3. The geometry of the computational domain. Gravity is aligned with the *x*-axis. The blue region depicts the approximate location of the convectively unstable layer at the start of the simulation, while the surrounding green volumes depict the locations of the bounding stably stratified layers.

are reduced by a common damping factor, *f*, resulting in damped velocities over the damping region, $v_d = f v$. The damping factor is defined as

$$f = (1 + \delta t \, \omega f_d)^{-1}, \qquad (7)$$

where δt is the time-step of the simulation, $\omega = 0.01$ is the damping frequency and is a free parameter chosen to correspond to a small fraction of the convective turnover. $f_d = 0.5 \, (\cos(\pi r/r_0) + 1)$, where *r* is the radial position in the vertical direction and $r_0 = 0.6 \times 10^9$ cm is the edge of the damping region in the vertical direction. Using this damping function, $f_d = 0$ at $r = r_0$, where the damping region starts. This ensures a smooth transition between the non-damped and damped regions.

To test the dependence of our results on numerical resolution, we simulated the carbon shell at four different resolutions. These models are named according to their resolution: `lrez - 128`³, `mrez - 256`³, `hrez - 512`³, and `vhrez - 1024`³.

Whether a computed flow will exhibit turbulence depends on the spatial and temporal discretization that is used. In the following, we explore heuristically the 3D modelling of turbulence on a discrete grid.

3.2.1 Spatial zoning considerations

A useful dimensionless number for determining the degree of turbulence in a simulation is the effective or *numerical* Reynolds number, a discrete analogue of the Reynolds number. It can be defined using the following arguments.

Kolmogorov (1941) showed that the rate of energy dissipation at any length-scale, λ (between the inertial range and Kolmogorov scale), is given by $\epsilon_\lambda \sim v_\lambda^3/\lambda$, where v_λ is the flow velocity at that scale. This relation can be applied at the extreme scales of the simulation, i.e. at the integral scale and the grid scale to give

$$\epsilon_\ell = \frac{v_{\rm rms}^3}{\ell} \quad \text{and} \quad \epsilon_{\Delta x} = \frac{\Delta u^3}{\Delta x}, \quad \text{respectively,} \qquad (8)$$

where Δu is the flow velocity across a grid cell. This velocity can also be used to define an effective numerical viscosity at the

grid scale

$$\nu_{\rm eff} = \Delta u \Delta x. \qquad (9)$$

For a turbulent system within a statistically steady state, Kolmogorov (1962) showed that the rate of energy dissipation is equal at all scales. Applying this equality to equation (8) yields (with the use of equation 9)

$$\nu_{\rm eff} = v_{\rm rms} \ell \left(\frac{\Delta x}{\ell}\right)^{4/3}. \qquad (10)$$

Therefore, the effective Reynolds number can be expressed as

$$\text{Re}_{\rm eff} = \left(\frac{\ell}{\Delta x}\right)^{4/3} \sim N_x^{4/3}, \qquad (11)$$

where N_x is the number of grid points in the vertical direction. In these simulations, this is a slight overestimate as in the vertical direction only half of the grid points represent the convective region.

Within the ILES paradigm, the effective Reynolds number is therefore limited by the momentum diffusivity[5] at the grid scale (equation 9), and as demonstrated by equation (11), it is the choice of spatial zoning that sets an upper limit on the degree of turbulence. The effective Reynolds numbers of our simulations ($N_x = 128–1024$) therefore range from around 650 to 10^4, suggesting that we are within the turbulent regime ($\text{Re}_{\rm eff} \gtrsim 1000$) for the finer grids.[6]

3.2.2 Time-scale considerations

The convective turnover time, τ_c (twice the transit time), is the time needed to set up the turbulent velocity field (Meakin & Arnett 2007b), following the initial perturbations in temperature and density. Therefore, *the convective turnover time is the minimum time-scale required for simulating turbulence*. For carbon burning, the turnover time is $\tau_c \sim 6.7 \times 10^3$ s. The maximum time-step size allowed by the explicit hydrodynamic solver is $\Delta t_{\max} = \Delta x/c_s$, where the sound speed is approximately $c_s \sim 4.5 \times 10^8$ cm s^{-1}. Therefore, the minimum number of time-steps needed to simulate a convective turnover time is $N_{\Delta t} \sim N_x/\text{Ma} = c_s \tau_c/\Delta x$ for Mach number Ma. For the `hrez` zoning ($N_x = 512$), the required number of time-steps equates to 8.2×10^5, which would exceed the available computer resource budget.

Hence, as one may guess intuitively, the modelling of smaller velocities requires more time-steps. One option to overcome this issue is to scale the velocity up by scaling the nuclear energy generation rate. Scaling the burning rate by a factor of 1000 (this only scales the velocity up by a factor of 10) reduces the convective turnover time to $\tau_c \sim 670$ s, and the minimum number of time-steps required to establish a turbulent flow decreases to $N_{\Delta t} \sim 8.2 \times 10^4$, for the `hrez` zoning, which is comfortably attainable given the available computational resources.

3.2.3 Boosting factor

A boosting factor of 10^3 for the nuclear energy generation rate was chosen in order for the simulations to match the turbulent driving

---

[5] The actual numerical dissipation of the PPM method is highly complex and non-linear (Sytine et al. 2000); the highest resolution simulations presented here seem to capture the effective dissipation accurately.

[6] This is supported by visual comparison of our simulations with experimental data (e.g. van Dyke 1982).
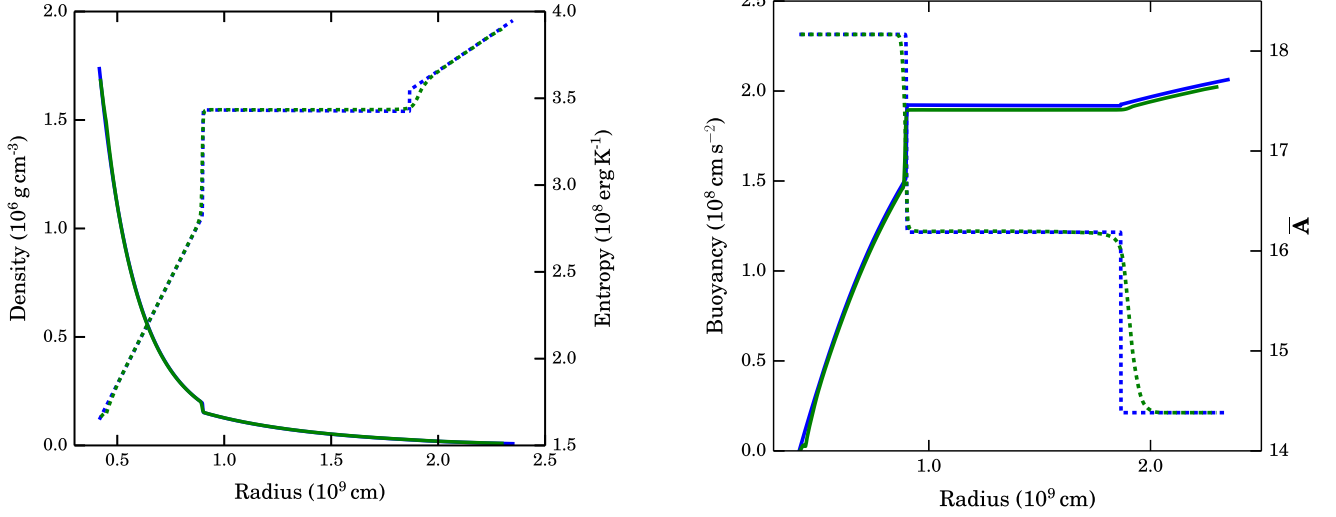
Figure 4. Left: initial radial density (solid) and entropy (dashed) profiles. Right: initial radial buoyancy (solid) and composition (dashed) profiles. 1D stellar evolution profiles calculated using GENEC (blue) are compared with the same profiles integrated and mapped on to the Eulerian Cartesian grid in PROMPI (green).

observed in oxygen-shell-burning simulations ($\sim 10^{12}$ erg g^{-1} s^{-1}; Meakin & Arnett 2007b).

In such simulations, there is no need to worry about the effect that such a boost in driving will have on the thermal diffusion in the model as it can be safely ignored in the bulk of the convective zone. This is because thermal diffusivity is negligible in comparison to the loss of heat through escaping neutrinos produced in the plasma (Arnett 1996, pp. 284–292), and so thermal diffusion implicitly only becomes important at the sub-grid scale (see also discussion in Viallet et al. 2015). Although future studies are needed to confirm the Péclet number in the boundary layers, Arnett et al. (2015) argue that thermal diffusivity is also very small in the boundary regions of the oxygen-burning shell, which would also apply to our boosted carbon shell. They show that a large Péclet number leads to an adiabatic expansion of the convective boundary.

This boosting of the driving luminosity does not have any dynamical effect on the shell structure, given the short physical time-scales of the simulations. The convective velocities and boundary mixing rates will be increased though, compared to the astrophysical scenario being modelled. A key advantage to this approach is that more convective turnovers can be simulated for the given physical time that is being modelled, but it does highlight an important sensitivity of the hydrodynamic flow to the numerical set-up. Additionally, as the nuclear luminosity has been boosted the neutrino losses contribute negligibly to the thermal evolution of the model.

3.3 Initial conditions and runtime parameters

The initial vertical extent of the convective region (0.90×10^9 cm $\lesssim x \lesssim 1.87 \times 10^9$ cm) can be seen through the entropy, buoyancy, and composition profiles in Fig. 4. The convective region is apparent through the homogeneity of these quantities due to strong mixing, while the boundaries are defined by sharp jumps.

An initial hydrostatic structure in PROMPI was reconstructed from the entropy, composition, and gravitational acceleration profiles taken from the GENEC 1D model. Stellar models do not have regularly spaced mesh points in the radial direction given the fact that they use a Lagrangian method and so the spatial resolution is sometimes coarse, especially at convective boundaries. For this reason,

the 1D GENEC profiles of the entropy (s), average atomic mass ($\bar{A}$), and average atomic number ($\bar{Z}$) were first remapped on to a finer grid mesh before linearly interpolating on to the Eulerian grid in PROMPI. The details of this remapping can be found in Appendix B.

There is no nuclear-burning network in this model, in the sense that we do not follow the depletion of ^{12}C through nuclear burning, but only through mixing. The abundance variables $\bar{A}$, $\bar{Z}$, and $X_{^{12}C}$ are somewhat redundant though, as the electron fraction $Y_e = \bar{Z}/\bar{A}$ does not change.

To ensure the model is in hydrostatic equilibrium, the density $\rho(s, p, \bar{A}, \bar{Z})$ was integrated along the new radial grid according to:

$$\frac{\partial \rho}{\partial r} = \frac{\mathrm{d}s}{\mathrm{d}r}\left(\frac{\partial \rho}{\partial s}\right)_{p,\bar{A},\bar{Z}} + \frac{\mathrm{d}p}{\mathrm{d}r}\left(\frac{\partial \rho}{\partial p}\right)_{s,\bar{A},\bar{Z}} + \frac{\mathrm{d}\bar{A}}{\mathrm{d}r}\left(\frac{\partial \rho}{\partial \bar{A}}\right)_{s,p,\bar{Z}}$$
$$+ \frac{\mathrm{d}\bar{Z}}{\mathrm{d}r}\left(\frac{\partial \rho}{\partial \bar{Z}}\right)_{s,p,\bar{A}}, \tag{12}$$

the second term is simplified by enforcing hydrostatic equilibrium to within a tolerance of 10^{-10}, given by:

$$\frac{\mathrm{d}p}{\mathrm{d}r} = -\rho g. \tag{13}$$

For our plane-parallel geometry set-up, the gravitational acceleration was parametrized by a function of the form $g(r) = A/r$, with constant $A = 1.5 \times 10^{17}$ cm^2 s^{-2}. The total derivatives $\mathrm{d}s/\mathrm{d}r$, $\mathrm{d}\bar{A}/\mathrm{d}r$, and $\mathrm{d}\bar{Z}/\mathrm{d}r$ were calculated from the fitted profiles introduced earlier. The partial derivatives $\partial\rho/\partial s$, $\partial\rho/\partial p$, $\partial\rho/\partial\bar{A}$, and $\partial\rho/\partial\bar{Z}$ were calculated using the Helmholtz EOS (Timmes & Arnett 1999; Timmes & Swesty 2000). Fig. 4 shows the density, entropy, buoyancy, and average atomic mass profiles for the stellar model initial conditions, and the corresponding initial profiles that were mapped on to the Eulerian grid in PROMPI.

Simulation time is typically measured in convective turnovers, $\tau_c = 2\,\ell_c/v_{\rm rms}$, where ℓ_c is the height of the convective region and $v_{\rm rms}$ is the global convective velocity, $v_{\rm rms} = \sqrt{\langle v_x^2 \rangle - \overline{\langle v_x \rangle}^2}$ (see Appendix C for a description of this notation). Our simulations typically span 3–4 turnovers, following an initial transient phase of around 1000 s.

Table 1. Summary of simulation properties. N_{xyz}: total number of zones in the computational domain ($N_x \times N_y \times N_z$), τ_{sim}: simulated physical time (s), v_{rms}: global rms convective velocity (cm s^{-1}), τ_c: convective turnover time (s), Ri_B: bulk Richardson number (values in brackets are representative of the lower convective boundary region), and Ma: Mach number.

	lrez	mrez	hrez	vhrez
N_{xyz}	128^3	256^3	512^3	$1{,}024^3$
τ_{sim}	3,213	3,062	2,841	986
v_{rms}	3.76×10^6	4.36×10^6	4.34×10^6	3.93×10^6
τ_c	554	474	471	513
Ri_B	29 (370)	21 (259)	20 (251)	23 (299)
Ma	0.0152	0.0176	0.0175	0.0159

Convection is seeded in the hydrodynamic models through random perturbations in temperature and density in the same manner described by Meakin & Arnett (2007b) who also showed that the subsequent nature of the flow was independent of these seed perturbations. For the vhrez model, convection was not seeded through perturbations in the 1D stellar model initial conditions, but was restarted from the hrez model at 980 s, this was done by duplicating each of the cells to double the resolution. Due to limited computational resources available for this study, the vhrez model was not simulated for enough convective turnovers in order for the temporal averaging to be statistically valid. As a result, we only included this model in part of our detailed analysis.

4 SIMULATION RESULTS

A summary of the simulation models is presented in Table 1, which includes the number of zones, physical time simulated, convective velocity, convective turnover time, bulk Richardson number, and convective Mach number.

4.1 The onset of convection and time evolution

The temporal evolution of the global (averaged over the convective zone) specific kinetic energy for all of the models is presented in Fig. 5. The first ∼1000 s of evolution are characterized by an initial transient associated with the onset of convection. By ∼1250 s, all of the models settle into a quasi-steady state characterized by semiregular pulses in kinetic energy occurring on a time-scale of the order of a convective turnover time. These pulses are associated with the formation and eventual breakup of semicoherent, large-scale eddies or plumes that traverse a good fraction of the convection zone before dissipating, and is a phenomena that is typical of stellar convective flow (Meakin & Arnett 2007b; Arnett & Meakin 2011a,b; Viallet et al. 2013; Arnett et al. 2015).

As discussed in Section 3.3, the evolution of the highest resolution model, vhrez, begins at ∼1000 s, when it was restarted from model hrez by simply sampling the underlying flow field on to a higher resolution mesh. As is typical of turbulent flow, this model relaxes in approximately one large-eddy crossing time as evidenced by the re-establishment of the TKE balance discussed below (Section 4.4).

Although these simulations do not sample a large number of convective turnover times (between ∼2 and ∼6; discussed below), resolution trends are still apparent. The most prominent trend seen here is the kinetic energy peak associated with the initial transient, which increases as the grid is refined. This is not linked to the initial seed perturbations and is most likely related to the decreased numerical dissipation at finer zoning.
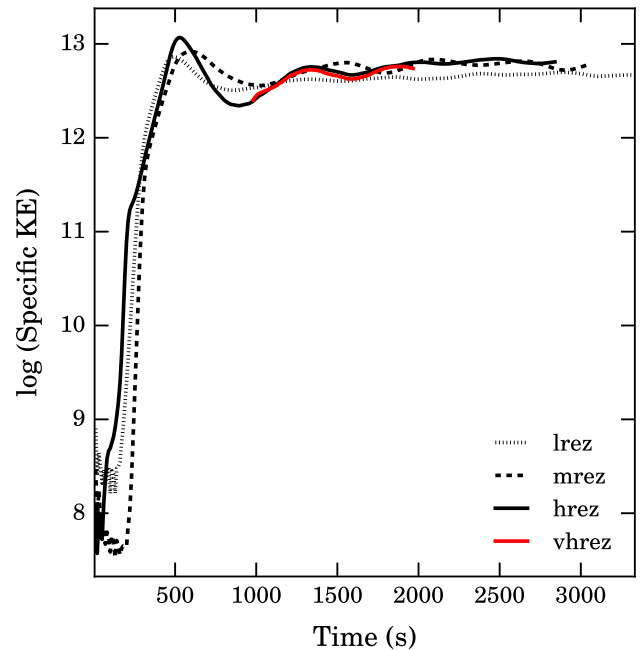

Figure 5. Temporal evolution of the global specific kinetic energy: thin dashed – lrez; thick dashed – mrez; black solid – hrez; and red solid – vhrez. The quasi-steady state begins in each model after approximately 1000 s, and only the lrez model kinetic energy appears to have a dependence on the resolution.

A similar trend can also be seen in the quasi-steady turbulent state that follows the initial transient. Interestingly, in this case, a resolution dependence only appears to manifest for the lowest resolution model, lrez. This has an overall smaller amplitude of kinetic energy as well as a much smaller variance associated with the formation and destruction of pulses. These properties can be naturally attributed to a higher numerical dissipation at a lower resolution, an issue that we return to throughout the remainder of the paper.

4.2 Properties of the quasi-steady state

Rms fluctuations in density, pressure, entropy, temperature, and composition centred around their mean background states are shown for the hrez model in the left-hand panel of Fig. 6. Fluctuations in the convective region are small and of a similar magnitude for all quantities except the composition. Near the convective boundary regions, the relative amplitude of the fluctuations is highest, reaching values around 1 per cent of the mean background state.

Pressure fluctuations can be grouped into a compressible and an incompressible components. The former describes the acoustic nature of pressure fluctuations such as when the flow turns and is compressed. The latter describes the advective nature of pressure perturbations due to buoyancy effects. The compressible component of the pressure fluctuations is proportional to a pseudo-sound term, $\rho_0 \, v'^2/p_0$, shown by the dashed line in the left of Fig. 6. This term is highest in the convective region and has a magnitude similar to the square of the Mach number, ∼3×10^{-4}.

Horizontally averaged rms velocity components for the hrez model are shown on the right of Fig. 6. These profiles represent an average over the quasi-steady-state period of the simulation, which we estimate to occur over four convective turnover times. The total
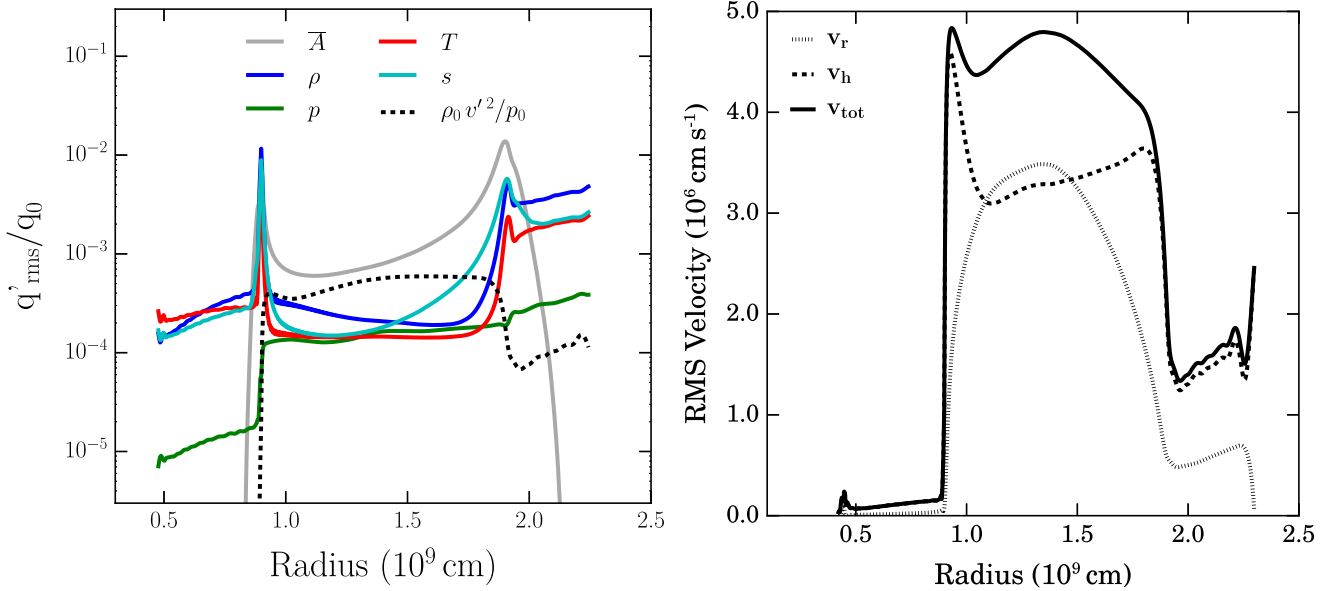
Figure 6. Left: horizontally averaged rms fluctuations of composition, density, pressure, temperature, and entropy weighted by their average values. The dashed curve represents a pseudo-sound term. These fluctuations were time averaged over four convective turnover times of the `hrez` model. Right: rms radial (thin dashed), horizontal (thick dashed), and total (solid) velocity components, time averaged over four convective turnover times for the `hrez` model. Local maxima in the horizontal velocity indicate the approximate convective boundary locations.

rms velocity reaches a maximum of around 4.8×10^6 cm s^{-1} both in the centre of the convective region ($x \sim 1.4 \times 10^9$ cm) and also near the lower convective boundary ($x \sim 0.9 \times 10^9$ cm). Contributions to the total velocity are dominated by the radial velocity over the central part of the convective region, while close to the convective boundaries the horizontal velocity ($v_h = \sqrt{v_y^2 + v_z^2}$) is the largest component. The local maxima in horizontal velocities correspond to the radial deceleration and eventual turning of the flow near the convective boundaries. Such features are typical of shallow convective regions and are similarly reported in simulations of the oxygen-burning shell by Meakin & Arnett (2007b) and Jones et al. (2017), see their figs 6 and 11, respectively.

The components of the flow velocity for the `hrez` model are illustrated by 2D colour maps in Fig. 7. These snapshots of the flow were taken at 1480 s into the simulation, where the quasi-steady state has already developed. Each vertical 2D slice in Fig. 7 is taken at the same horizontal (z) position in the x–y plane, at $z = 0.94 \times 10^9$ cm (i.e. in the middle of the domain, see Fig. 3 for the domain geometry). The left-hand, middle, and right-hand panels show the x, y, and z components of the velocity, respectively. In the left-hand panel, strong, buoyant up-flows are shown in shades of red, while cooler, dense down drafts are shown in shades of blue.

The convective boundaries are apparent in all the velocity components from the sudden drop in magnitude. The lower convective boundary is clearly distinguishable, but the upper boundary is more subtle with velocities above the boundary represented by slightly lighter shades of red and blue. In the middle and right-hand panels, horizontal velocities are strongest near the convective boundaries (shown by extended patches of dark red and dark blue colours), this is indicative of the flow turning as it approaches the boundary. Gravity mode waves excited by turbulence in the convective region can be seen in the stable region above, and are shown by lighter shades of red and blue in the upper part of each panel.

4.3 Turbulent velocity spectrum

We investigate the degree to which our simulations are capturing the phenomenology of turbulence, including whether or not they have developed an inertial sub-range, by looking at velocity spectra of the modelled flows. Spectra were calculated using a 2D fast Fourier transform[7] of the vertical velocity in a horizontal plane at the mid-height of the convection zone. The results of this transform are presented in Fig. 8, where the square of the transform, $\overline{\hat{V}^2}(k)$ is plotted as a function of the wavenumber k. These spectra are time averaged over several convective turnovers, and a 1D profile is obtained by binning the 2D transform within the k_y–k_z plane, where k_y and k_z are the wavenumbers in the y- and z-directions, respectively ($k_y, k_z = 0, 2\pi, 4\pi, \ldots, 2\pi(N/2)$, where N is the number of grid points in one dimension, i.e. the resolution).

A scaling of $(k^{5/3}/N)$ is applied to the velocity spectrum to compensate for its $k^{-5/3}$ dependence in the inertial range (Kolmogorov 1941). A plateau in the velocity spectra can be seen in all of the models. This plateau extends over the largest range in wavenumbers for the `vhrez` (cyan) case, $10 \lesssim k \lesssim 500$. Although this plateau in the spectrum is not a formal proof of the existence of an inertial range, it supports the fact that our simulations (at least in the `hrez` and `vhrez` cases) resolve appropriately the various ranges of the problem.

These velocity spectra thus demonstrate that our two highest resolution PPM simulations posses essential characteristics of a turbulent flow – an integral scale, an inertial range obeying the $k^{-5/3}$ power law (at least for a sub-range of wavenumbers), and an effective Kolmogorov length-scale (represented by the grid scale). In our two lowest resolution runs, on the other hand, the plateau is either very short or not present, indicating that models with fewer than 512^3 zones are probably not very accurate models of turbulence. This minimum desired resolution is in reasonable agreement with

---
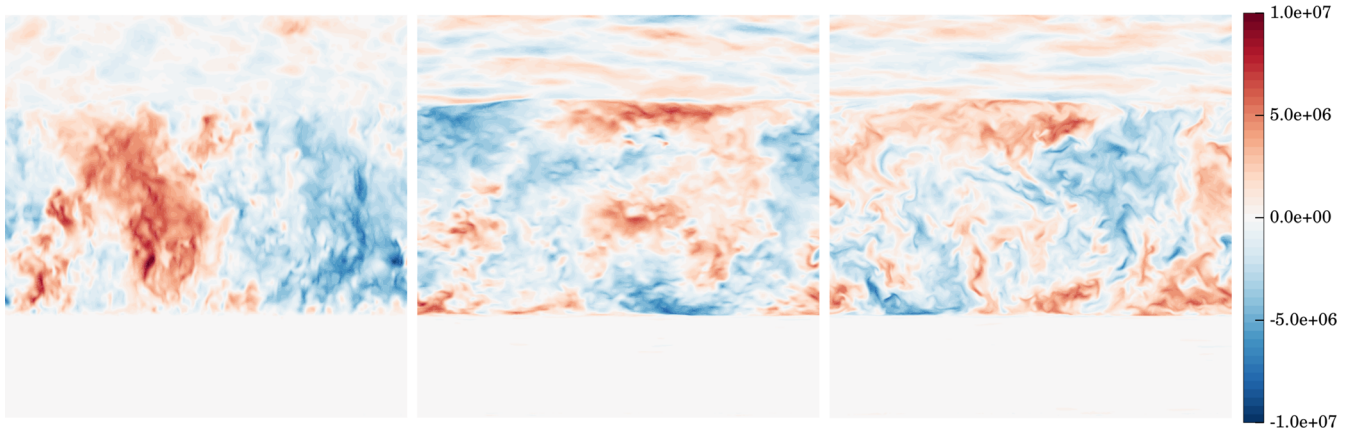
[7] Using the PYTHON package NUMPY.FFT.FFT2.

Figure 7. Vertical 2D slice (2D plane defined by $z = 0.94 \times 10^9$ cm, where z is one of the two horizontal directions in the PROMPI simulation) of velocity components, 1480 s into the `hrez` simulation. From left to right v_x (vertical component), v_y, and v_z (horizontal components) are plotted. Reds are positive, blues are negative, and white represents velocities around zero.
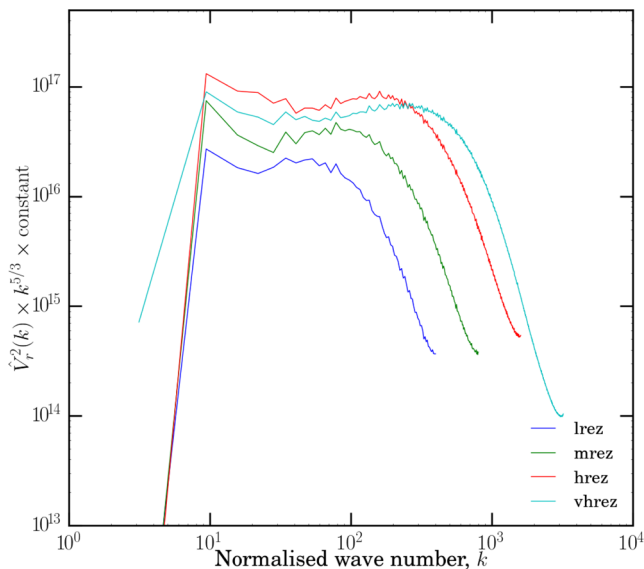

Figure 8. Specific kinetic energy spectrum of the four simulations. Spectra were obtained from a 2D Fourier transform of the vertical velocity (at the mid-height of the convective region), averaged over several convective turnovers. The vertical axis corresponds to the square of the Fourier transform, scaled by a 'Kolmogorov factor', $k^{5/3}$, and a constant (N^{-1}) to allow easier comparison between resolutions. This scaling highlights the sub-range of wavenumbers which obey the $k^{-5/3}$ power law (Kolmogorov 1941). The horizontal axis represents the wavenumber, k. See the text for more details.

our estimate of the numerical Reynolds number in Section 3.2.1 ($\mathrm{Re}_{\mathrm{eff}} \sim N_x^{4/3}$).

4.4 Mean field analysis of kinetic energy

A common method to study turbulent flows is to use the RANS equations. This reduction of multidimensional data into horizontal and time-averaged 1D radial profiles allows us to represent the data obtained from hydrodynamic simulations in the context of 1D stellar evolution models (Mocák et al. 2014).

We use the RANS framework to calculate the terms of the TKE equation (details given in Appendix C) and to analyse them. Momentum diffusion is not included in our simulations as we solve

the inviscid Euler equations within the ILES paradigm. Instead, we infer TKE dissipation through the truncation errors that arise due to discretizing these equations (Grinstein, Margolin & Rider 2007), this provides us with an effective numerical dissipation (ϵ_k in equation C4), which we compute from the residual energy in the TKE budget.

4.4.1 Time-averaged properties of the TKE budget

The profiles of the mean TKE equation terms (equation C4) for the `lrez`, `hrez`, and `vhrez` models are shown in the left-hand panels of Fig. 9, with the inferred viscous dissipation shown by a black dashed line. These profiles are time integrated over multiple convective turnovers and normalized by the surface area of the domain. Bar charts of the mean fields integrated over the domain are shown in the right-hand panels. Comparing the left-hand panels of Fig. 9 to fig. 8 of Viallet et al. (2013), we see that the energetic properties of convection during carbon burning are very similar to oxygen burning.

Time evolution. The Eulerian time derivative of the kinetic energy, $\rho \mathbf{D}_t E_k$, is small or negligible over the simulation domain, implying that over the chosen time-scale the model is in a statistically steady state.

Transport terms. The transport of kinetic energy throughout the convective region is determined by the two transport terms, the TKE flux, $\mathbf{F_k}$, and the acoustic flux, $\mathbf{F_p}$ (see Viallet et al. 2013, for a detailed discussion on these terms).

Source terms. Turbulence is driven by two kinetic energy source terms, $\mathbf{W_b}$ and $\mathbf{W_p}$. The rate of work due to buoyancy, $\mathbf{W_b}$ (density fluctuations), is the main source of kinetic energy within the convective region, while $\mathbf{W_p}$, the rate of work due to compression (pressure fluctuations or pressure dilatation) is small. In the convective zone, we generally have $\mathbf{W_b} > 0$, as expected since it is the main driving term. Near the boundaries, however, there is a region where $\mathbf{W_b} < 0$. These regions are where the flow decelerates (braking layer) as it approaches the boundary, as already found and discussed for oxygen burning in Meakin & Arnett (2007b) and Arnett et al. (2015). We note that the top braking layer is more extended than the bottom one. The top convective boundary width is also more extended. We come back to this point in Section 4.5.3.

Dissipation. Kinetic energy driving is found to be closely balanced by viscous dissipation, ϵ_k; a property consistent with the statistical steady state observed. The time- and horizontally averaged
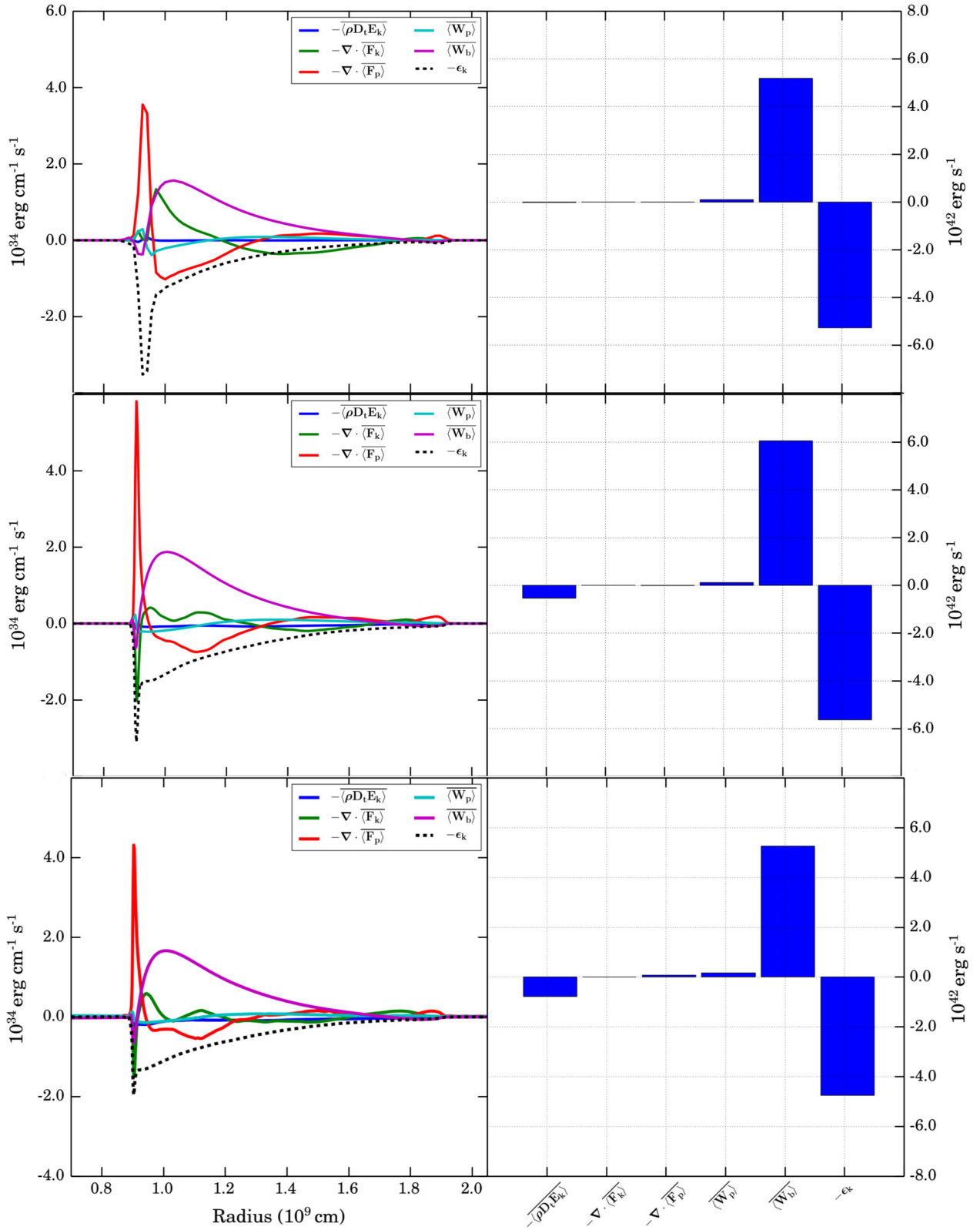
Figure 9. Left: decomposed terms of the mean kinetic energy equation (equation C4), which have been horizontally averaged, normalized by the domain surface area, and time averaged over the steady-state period. Time averaging windows are over 2200, 1850 and 1000 s for the `lrez` (top), `hrez` (middle), and `vhrez` (bottom) models, respectively. Right: bar charts representing the radial integration of the profiles in the left-hand panel. This plot is analogous to the middle panels of fig. 8 in Viallet et al. (2013).
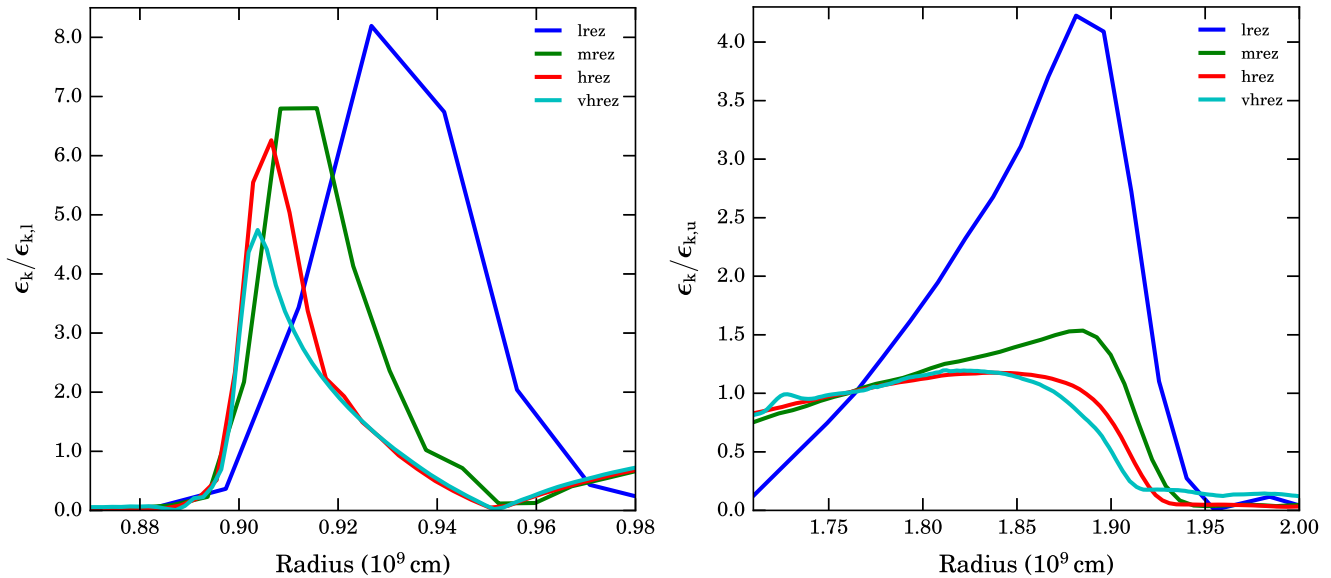
Figure 10. Numerical dissipation inferred from the residual TKE for the lower (left) and upper (right) convective boundary regions in the `lrez`, `mrez`, `hrez`, and `vhrez` models. The dissipation at each boundary has been normalized by a value at a common position within the convective region near to the boundary. The `hrez` and `vhrez` residual profiles appear to be converging at the upper boundary, suggesting that the representative numerical dissipation here is physically relevant.

dissipation can be seen to extend roughly uniformly throughout the convective region, but increases slowly in its amplitude with depth, tracking the rms velocities. There is almost no dissipation in the stable layers, where velocity amplitudes are low and turbulence is absent. Finally, there are notable peaks in dissipation localized at the convective boundaries. The dependence of these peaks on resolution is discussed next.

4.4.2 Resolution dependence

We compare models of three different resolutions – the `lrez`, `hrez`, and `vhrez` models, to determine if any of the physical results depend on the chosen mesh size. Over the three resolutions, we find qualitatively similar results but there is significant deviation at the lower boundary region ($\sim$0.9 $\times$ 10^9 cm). A key question is whether or not our higher resolution models are able to capture the physics at boundaries accurately.

At the lower convective boundary ($\sim$0.9 $\times$ 10^9 cm), a peak in dissipation appears at all resolutions (see dashed line in left-hand panels of Fig. 9). The peak decreases in amplitude and width with increasing resolution, indicating that the models are not converged numerically.

A comparison of the dissipation in this region for all resolutions is given in the left-hand panel of Fig. 10. Here, the TKE dissipation is normalized by a value at a common position within the convective region near to the boundary. This highlights the relative decrease in this numerical peak with respect to a converged value in the convective region. A similar plot for the upper boundary is presented in the right-hand panel of Fig. 10 shows that the dissipation at the boundary is smooth for both `hrez` and `vhrez` models. While in all cases, the dissipation curves contain some variance due to the stochastic nature of the flow, the trend with resolution is clear.

4.5 Convective boundary mixing

Entrainment events (similar to entrainment events found for oxygen burning, see e.g. fig. 23 in Meakin & Arnett 2007b) in the `hrez`

model can be seen in the left-hand panel of Fig. 11 (see e.g. bottom left of convective zone where material from below the convective zone is entrained upwards or top corners of the convective zones where the material is entrained from the top stable layer). The left-hand panel shows the average atomic weight fluctuations relative to their mean, with the velocity field in the (x, y) plane overplotted (the vertical axis corresponds to the radial/vertical direction, see Fig. 3). The right-hand panel also shows the velocity magnitude ($\sqrt{v_x^2 + v_y^2}$) for the same snapshot of the `hrez` model. In both panels, strong flows can be seen in the centre of the convective region and shear flows can be seen over the entire convective region. These shear flows have the greatest impact at the convective boundaries, where composition and entropy are mixed between the convective and radiative regions. Turbulent entrainment within the convective shell can also be inferred through the radial profile of the buoyancy work, whereby the positive work near the boundaries (e.g. the magenta curve of Fig. 9 at $\sim$0.9 $\times$ 10^9 cm) implies that TKE of overturning fluid elements near the boundary does work against gravity to draw stable material into the convective region. This characteristic is explained in detail and seen in the buoyancy flux profiles of the oxygen-burning shell in Meakin & Arnett (2007b) (see their section 7.2 and the top panel of fig. 25). This is a very different picture from the parametrizations that are used to describe convective boundary mixing in most modern 1D stellar evolution models.

In this section, we start by estimating the position (and its time evolution) and thickness of the boundaries. We then interpret the time evolution of the boundary positions in the framework of the entrainment law. Finally, we compare the upper and lower boundaries.

4.5.1 Estimating convective boundary locations

Entrainment at both boundaries pushes the boundary position over time into the surrounding stable regions. In order to calculate the boundary entrainment velocities, first the convective boundary positions must be determined in the simulations. In the 3D simulations,
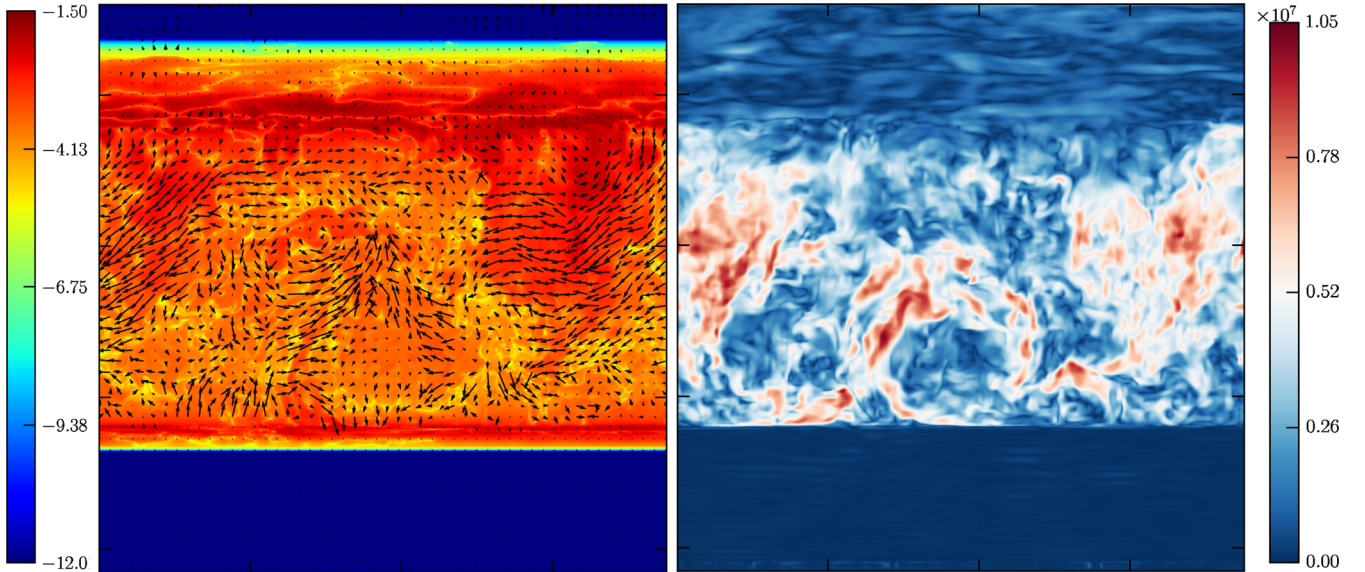
Figure 11. Left: vertical cross-section of the absolute average atomic weight fluctuations relative to their mean within the convective region. The colour map represents the logarithm of compositional fluctuations ($|\overline{A}'/\overline{A}_0|$) relative to the mean. Arrows show the vertical component and one horizontal component of the velocity vector field, (v_x, v_y) (the vertical axis corresponds to the radial/vertical direction, see Fig. 3). The direction of the arrows indicates the direction of this vector field in the x–y plane, and their length the magnitude of the velocity vector, $\sqrt{v_x^2 + v_y^2}$, at that grid point. Right: vertical cross-section of the same velocity vector field plotted as arrows in the left-hand panel. The colour map represents the velocity magnitude in cm s^{-1}. Both snapshots were taken at 2820 s into the `hrez` simulation. A movie of the velocity magnitude is available on this webpage: http://www.astro.keele.ac.uk/shyne/321D/convection-and-convective-boundary-mixing/visualisations/very-high-resolution-movie-of-the-c-shell/view.

the boundary is a 2D surface and is not spherically symmetric as in 1D stellar models. In order to estimate the radial position of a convective boundary we first map out a 2D horizontal boundary surface, $r_{j,k} = r(j, k)$, for $j = 1$, n_y; $k = 1$, n_z, where n_y and n_z are the number of grid points in the horizontal y- and z-directions. We estimate the radial position of the boundary at each horizontal coordinate to coincide with the position where the average atomic weight, $\overline{A}$, is equal to the average between the mean value of $\overline{A}$ in the convective and the corresponding radiative zones as defined in equation (A3). The standard deviation of the position, σ_r, represents the amplitude of the fluctuations of the vertical position of the boundary across the horizontal plane due to the fact the boundary is not a flat surface. Our method is a valid but not a unique way in which to calculate the boundary position. See Sullivan et al. (1998), Fedorovich, Conzemius & Mironov (2004), Meakin & Arnett (2007b), Liu & Ecke (2011), Sullivan & Patton (2011), van Reeuwijk, Hunt & Jonker (2011), Garcia & Mellado (2014), and Gastine, Wicht & Aurnou (2015) for a discussion of alternative definitions. The time evolution of the boundary position and its standard deviation are plotted in Fig. 13.

4.5.2 Convective boundary structure

While stellar evolution codes describe a convective boundary as a discontinuity (see the composition profile in the right-hand panel of Fig. 4, for example), 3D hydrodynamic simulations show a more complex structure. A boundary layer structure is formed between the convective and stably stratified regions. This can be seen from the apparent structure of the mean fields, at $\sim 0.9 \times 10^9$ and $\sim 1.9 \times 10^9$ cm, in the left-hand panels of Fig. 9, which represent the approximate locations of the lower and upper convective boundaries, respectively.

The buoyancy in the convective boundary regions is negative, as seen in the $\mathbf{W_b}$ profiles of Fig. 9. In these regions, approaching

fluid elements are decelerated and radial velocities greatly reduced. As horizontal velocities increase, the plumes turn around and fall back into the convective region. This is similar to the description by Arnett et al. (2015, see their fig. 5 and text therein).

4.5.3 Convective boundary thickness estimates

We estimate the thickness of the convective boundaries using the jump in composition, $\overline{A}$, between convective and stable regions. We denote the average composition (averaging removes stochastic fluctuations in composition) in the, lower stable, convective, and upper stable regions as, $\overline{A}_l$, $\overline{A}_c$, and $\overline{A}_u$, respectively. We consider the boundary region to extend between 99 per cent and 101 per cent of the respective positions coincident with such compositional values. For each boundary, we signify such values by the appendage of a subscript $-$ (99 per cent) or $+$ (101 per cent) to the composition of each region. Explicitly, the lower boundary thickness is defined as,

$$\delta r_l = r\left(\overline{A}_{c_+}\right) - r\left(\overline{A}_{l_-}\right). \tag{14}$$

The upper boundary thickness is similarly defined as,

$$\delta r_u = r\left(\overline{A}_{u_+}\right) - r\left(\overline{A}_{c_-}\right). \tag{15}$$

In addition, we also considered defining the boundary thickness using gradients in composition and entropy, and the jump in entropy at the boundary. We found that these other methods gave quantitatively similar results. In Fig. 12, we illustrate the estimation of the boundary thickness using equations (14) and (15) for the final time-step of each simulation. The radius of each profile has been shifted, such that the boundary position, $\overline{r}$ (see Section 4.5.1), of each model coincides with the boundary position of the `vhrez` model. With such a shift, it is easier to assess the dependence of the boundary shape on resolution.

The extents of the convective boundaries are marked by filled squares for each simulation. Filled circles represent the individual
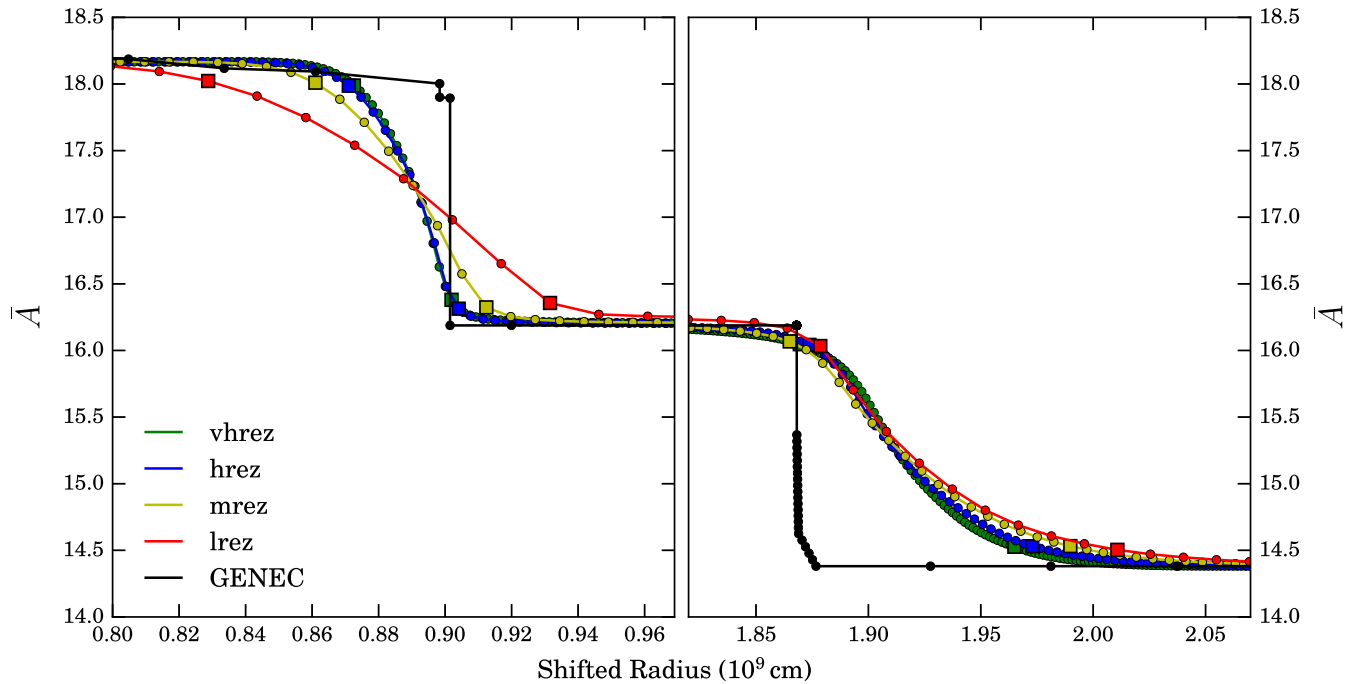
Figure 12. Radial compositional profiles at the lower (left) and upper (right) convective boundary regions for the last time-step of each model. The radius of each profile is shifted such that the boundary position, $\bar{r}$ (see Section 4.5.1), coincides with the boundary position of the vhrez model. In this sense, it is easier to assess the convergence of each model's representation of the boundary at the final time-step. Individual mesh points are denoted by filled circles. Approximate boundary extent (width) is indicated by the distance between two filled squares for each resolution. The initial composition profile calculated using GENEC is shown in black (for a qualitative comparison only). See the corresponding text (Section 4.5.3) for details of the definition of the boundary width.

Table 2. Table summarizing bulk and boundary region properties for each model. v_{rms} – global rms convective velocity (cm s^{-1}); ℓ_{c} – convective region height (cm); v_{e} – entrainment velocity (cm s^{-1}); δr – boundary region width (cm); $\delta r/H_{\mathrm{p}}$ – ratio of the boundary region width to the average pressure scaleheight across the boundary; τ_{b} – boundary entrainment time (s); and Ri$_{\mathrm{B}}$ – bulk Richardson number. Values in brackets correspond to the lower boundary.

	lrez	mrez	hrez	vhrez
v_{rms} (10^6)	3.76	4.36	4.34	3.93
ℓ_{c} (10^9)	1.08	1.04	1.03	1.09
v_e (10^4)	1.78 (−0.44)	2.01 (−0.39)	2.15 (−0.30)	1.59 (−0.46)
δr (10^7)	13.2 (10.3)	12.5 (5.1)	9.9 (3.3)	9.6 (2.9)
$\delta r/H_{\mathrm{p}}$	0.41 (0.36)	0.36 (0.17)	0.29 (0.11)	0.28 (0.10)
τ_b (10^3)	7.4 (23.4)	6.2 (13.1)	4.6 (11.0)	6.0 (6.3)
Ri$_{\mathrm{B}}$	29 (370)	21 (259)	20 (251)	23 (299)

mesh points, indicating the resolution of each simulation. Note that, the composition profile labelled as model GENEC is from the 1D stellar model, and was used as part of the initial conditions for all of the 3D models, so serves only as a qualitative comparison. The exact thickness of each boundary is shown in Table 2, along with their fraction of the local pressure scaleheight.

In Fig. 12 (right-hand panel), it can be seen that the composition gradient at the top boundary is nearly converged between all resolutions and varies only mildly between the lowest resolution case and

the other models. The composition gradient at the lower boundary (left-hand panel), on the other hand, varies significantly between the lrez and hrez models, while between the hrez and vhrez, the boundary shape appears to have nearly converged although is still narrowing slightly. These trends are confirmed by the quantitative estimates of the boundary widths presented in Table 2.

The thickness determined from the abundance gradients is larger than the standard deviation, σ_{r}, of the boundary location (corresponding to the mid-points of the abundance gradients plotted in Fig. 12) shown as shaded areas in Fig. 13. This is expected since the fluctuations of the boundary location do not take into account its thickness or width, but only the location of its centre (mid-point). These fluctuations of the boundary location can be compared to fluctuations in the height of the ocean surface due to the presence of waves. The fact that the width determined from the abundance gradients (given in Table 2) is significantly larger means that there is mixing across the boundary. A promising candidate for this type of mixing is the Kelvin–Helmholtz instability which would give rise to the shear motions seen in Fig. 14. This figure shows sequential slices of the flow velocity across the left section of the upper convective boundary region. Such shear mixing is induced by plumes rising from the bottom of the convective region and turning around at the boundary (see also the shear layer in fig. 5 of Arnett et al. 2015). Mixing also occurs through plume impingement or penetration with the boundary. Some mixing may also occur through the presence of gravity waves which propagate through the stable region. It is not expected that the upper boundary gradient will steepen, as this would support more violent surface waves whose non-linear dissipation would tend to broaden the gradient, resulting in a negative feedback loop between these two processes.
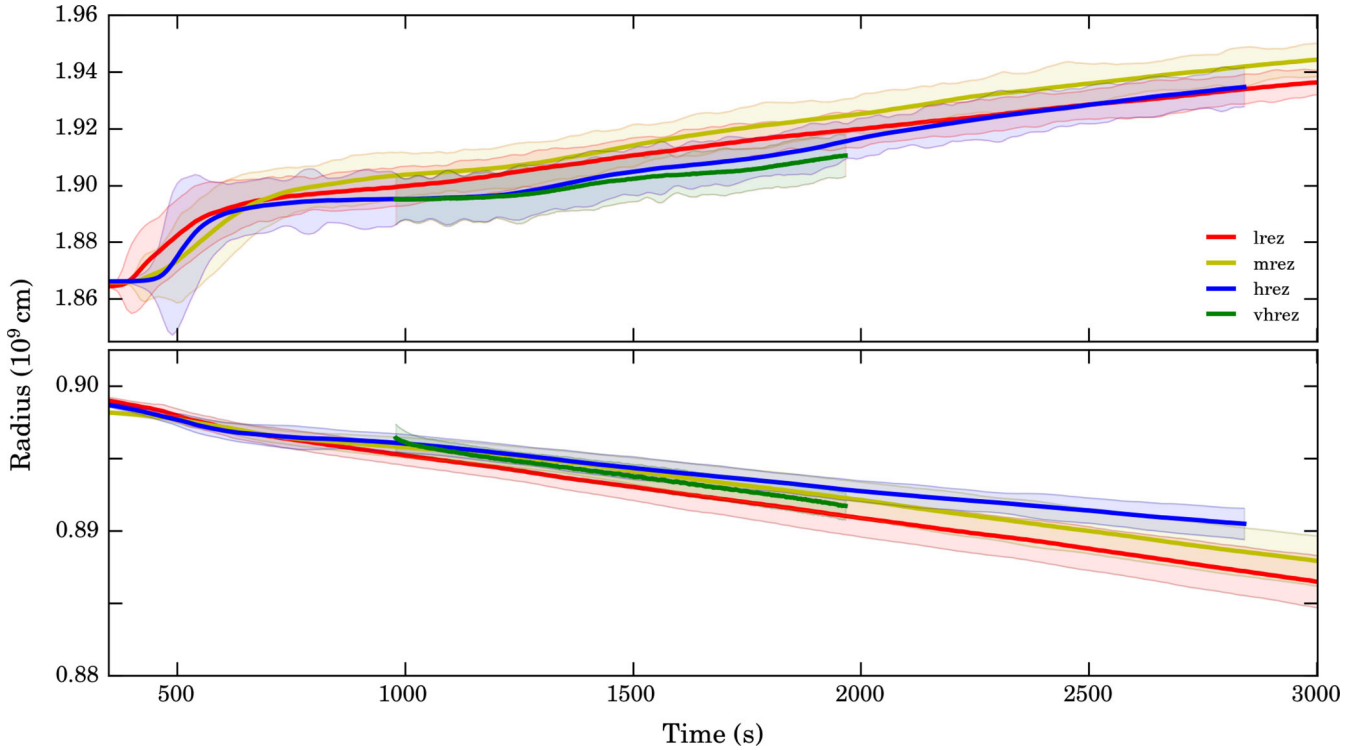
Figure 13. Time evolution of the mean radial position of the convective boundaries, averaged over the horizontal plane for all four resolutions. Shaded envelopes are twice the standard deviation from the boundary mean location. The convective turnover time in these simulations is of the order of 1000 s. Top panel: upper convective boundary region. For increasing resolution, the average standard deviation, σ_r, in the estimated boundary position are the following percentages of the local pressure scaleheight: 3.3 per cent; 3.8 per cent; 4.3 per cent; and 4.5 per cent. Bottom panel: lower convective boundary region. For increasing resolution, the average standard deviation in the estimated boundary position are the following percentages of the local pressure scaleheight: 0.8 per cent; 0.7 per cent; 0.4 per cent; and 0.6 per cent. These shaded areas represent the variation in the boundary height due to the fact that the boundary is not a flat surface. This can be compared to the surface of the ocean not being flat due to the presence of waves.

It is important to remember that the boundary widths given in Table 2 are only estimates. The key finding are (1) that the lower boundary has a narrower width compared to the upper, and (2) the widths are relatively well converged between the `hrez` and `vhrez` models.

4.5.4 Convective boundary evolution and entrainment velocities

The variation in time of the average surface position, $\bar{r}$, of both boundaries is shown for all models in Fig. 13. Positions are shown as solid lines and twice the standard deviation as the surrounding shaded envelopes. Following the initial transient ($>1000\,\mathrm{s}$), a quasi-steady expansion of the convective shell proceeds. We obtained the entrainment velocities, v_e, given in Table 2 using a linear fit to the time evolution of the boundary positions during the quasi-steady phase. These velocities are very high. If one multiplies them by the lifetime of carbon shell burning (of the order of 10 yr), the convective boundaries would move by more than 10^{10} cm, which would lead to dramatic consequences for the evolution of the star. Note, though, that the driving luminosity of the shell was boosted by a factor of 1000. We will come back to this point in Section 4.6.

4.5.5 The equilibrium entrainment regime

In the equilibrium entrainment regime (Fedorovich et al. 2004; Garcia & Mellado 2014), the time-scale for the boundary migration, τ_b, is comparable to or larger than the turbulent transit time-scale, τ_c (Section 3.3). Therefore, in this regime, the entrainment process is sampling the entire spectrum of turbulent motions over the inertial

range rather than being sensitive to individual turbulent elements, such as in strong, individual outlier's events. This simplifies the development of mixing models within this regime. The boundary entrainment velocity $v_e = \mathrm{d}\bar{r}/\mathrm{d}t$ is defined in terms of the mean boundary position $\bar{r}(t)$. We define the boundary mixing time-scale as $\tau_b = \delta r/|v_e|$, where δr is the boundary thickness (Table 2), which we define in Section 4.5.3. We find τ_b/τ_c ratios for the upper convective boundary of 13.4, 13.1, 9.8, and 11.7 for the `lrez`, `mrez`, `hrez`, and `vhrez` models, respectively, placing all of these boundaries firmly in the equilibrium regime.

4.5.6 The entrainment law

The time rate of change of the boundary position due to turbulent entrainment (the entrainment velocity), v_e, has been found to scale as a power of the bulk Richardson number for a wide range of conditions (e.g. Garcia & Mellado 2014). This relationship is often referred to as an *entrainment law* in the meteorological and atmospheric and is typically written as:

$$\frac{v_e}{v_{rms}} = A\,\mathrm{Ri}_B^{-n}. \tag{16}$$

Many LES (e.g. Deardorff 1980) and laboratory (e.g. Chemel, Staquet & Chollet 2010) studies have found similar values for the coefficient, A, typically between 0.2 and 0.25, although experimental measures have been more uncertain.

The exponent, n, is often found to be close to unity for convectively driven turbulence (e.g. Fernando 1991; Stevens & Lenschow 2001), a result that follows from basic energetic considerations. On
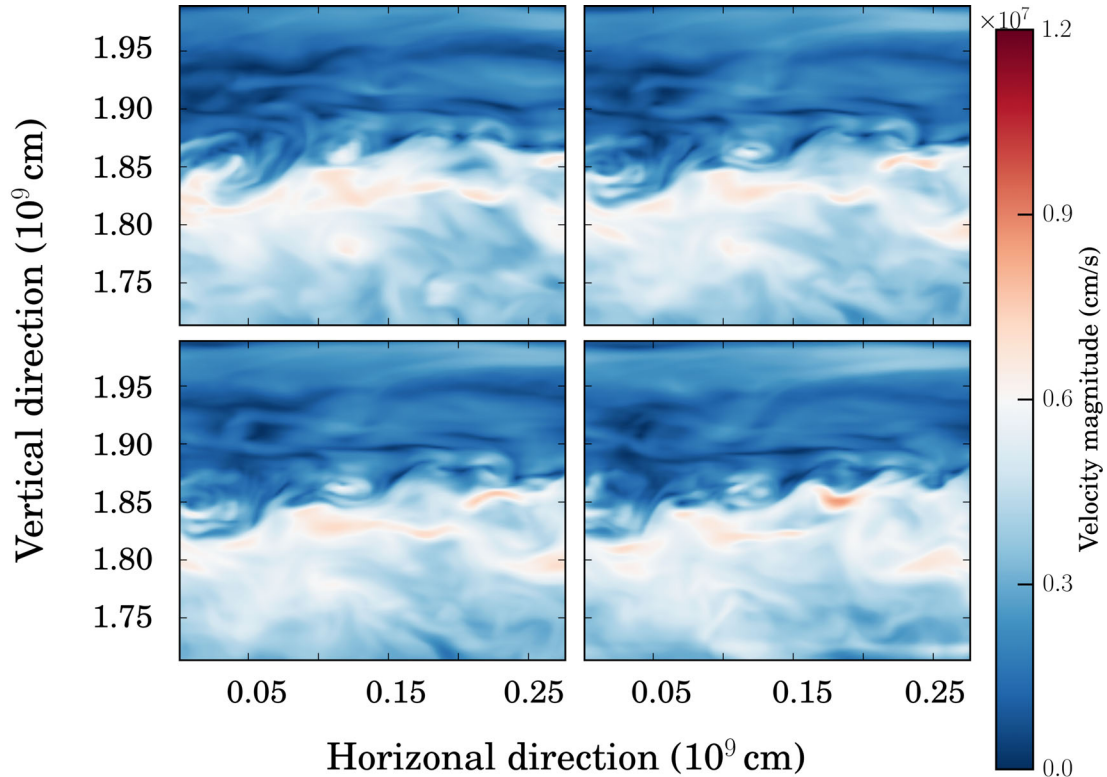
Figure 14. Sequential vertical cross-sections in the *x*–*y* plane of the velocity magnitude, $\sqrt{v_x^2 + v_y^2 + v_z^2}$, across the left section of the upper convective boundary for the `vhrez` simulation. Snapshots are taken at 1565 s (upper left), 1570 s (upper right), 1575 s (lower left), and 1580 s (lower right). The colour bar presents the values of the velocity magnitude in units of cm s^{-1}. Each panel reveals shear mixing occurring across the boundary interface. The Kelvin–Helmholtz instability is a promising candidate for generating this type of mixing.

the other hand, in a recent DNS study, Jonker et al. (2013) showed that $A \approx 0.35$ and $n = 1/2$ for shear-driven entrainment.

We compare the bulk Richardson number (equation A5) of our 3D simulations to the initial conditions from the 1D stellar model (Cristini et al. 2016) and 3D oxygen-burning simulations from Meakin & Arnett (2007b). From the 1D, 15 M$_\odot$ stellar model of Cristini et al. (2016) used as initial conditions in these simulations, the bulk Richardson numbers of the carbon-burning shell are $\mathrm{Ri}_B^u \sim 1440$ and $\mathrm{Ri}_B^l \sim 2.0 \times 10^4$ at the upper and lower convective boundaries, respectively. While, for our 3D `vhrez` model (see Table 2), we found $\mathrm{Ri}_B^u \sim 23$ and $\mathrm{Ri}_B^l \sim 299$. The lower values we obtain in 3D are mainly due to the fact that we boosted the luminosity by a factor of 1000. This is further discussed in Section 4.6.

The entrainment speed (normalized by the rms velocity) is plotted as a function of the bulk Richardson number in Fig. 15. Red points represent the data obtained in the study by Meakin & Arnett (2007b), the solid red line is a best-fitting power law to the data following a linear regression, and the red dashed lines show the error in the computed slope. Blue opaque points represent the values obtained in the `hrez` and `vhrez` models and blue transparent points are the values obtained in the `lrez` and `mrez` models. We obtain a best-fitting power law to the `hrez` and `vhrez` data and the extremes of their error bars, shown by the solid blue line and dashed blue lines, respectively. The corresponding intercept and slope of this best fitting denote the entrainment coefficient, $A = 0.03\,(\pm0.01)$, and entrainment exponent, $n = 0.62\,(+0.09/\,-0.15)$, respectively. The value we obtain for the entrainment exponent, n, falls between the two scaling relations ($1/2 \leq n \leq 1$). Our value for the coefficient, A, however, differs from all of the values found in the literature.
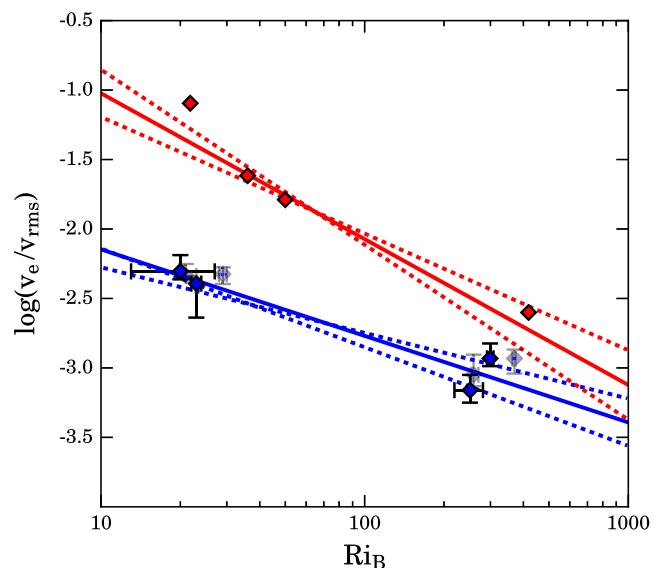

Figure 15. Logarithm of the entrainment speed for high Péclet number simulations, normalized by the rms turbulent velocity versus the bulk Richardson number. Red points represent data obtained in the study by Meakin & Arnett (2007b) and blue points represent data obtained in this study, transparent points represent the values for the `lrez` and `mrez` models, which are not included in best-fitting power law shown by the blue solid line. The blue dashed lines show the best fitting to the extremes of the error bars of the `hrez` and `vhrez` models. The red solid line is the best-fitting power law from a linear regression of the oxygen shell data and the red dashed lines show the error in the computed slope.

A larger data set is desired with which to explore in more detail the parameter space. Interestingly, the bulk Richardson numbers are similar between the carbon and oxygen shell models, and in particular, the lower convective boundaries both have higher values than the corresponding upper boundaries. The difference in the best-fitting values of A indicates that the oxygen shell is more efficient in converting kinetic energy into mixing. The difference in the best-fitting values of n indicates that there may be a second parameter besides Ri_B that is varying between the top and bottom of the convective shells, and in different ways, between the carbon and oxygen shell models. Finally, it must be reiterated that the ambiguity associated with calculating Ri_B is likely to account for some of the discrepancy.

4.5.7 Comparison of upper and lower convective boundary properties

Summarizing the boundary properties determined so far for the `hrez` model (see Table 2), the upper boundary region has a typical width of 9.9×10^7 cm, entrainment speed of 2.2×10^4 cm s^{-1}, and bulk Richardson number of 20. The lower boundary region typically has a width of 3.3×10^7 cm, entrainment speed of 3×10^3 cm s^{-1}, and bulk Richardson number of 251. We thus have a consistent picture of the lower boundary being narrower, having a slower entrainment velocity and being stiffer (higher Ri_B) compared to the upper boundary by a factor of about 3, 7, and 13, respectively.

4.6 Comparing convective boundary mixing between 1D and 3D models

Upon comparing our results to the 1D GENEC stellar evolution models, we find that our boundary widths are much larger and the boundary structures are very different from those calculated using strict Ledoux or Schwarzschild boundaries. The results of this and similar 3D hydrodynamic studies (Meakin & Arnett 2007b; Viallet et al. 2013; Woodward, Herwig & Lin 2015; Arnett et al. 2015; Couch et al. 2015; Jones et al. 2017) call for improved convective boundary mixing prescriptions in 1D stellar evolution models.

An approximate relation can be obtained between Ri_B and the luminosity, allowing the determination of convective boundary stiffness in 1D stellar models. Considering equation 16 (with $n = 1$), the relation $v_{rms} \propto L^{1/3}$ (assuming $\epsilon_{nuc} \sim v_{rms}^3/\ell$; Kolmogorov 1941, and $L = \int \epsilon_{nuc} \, dm$) and that the entrainment rate scales roughly linearly with the luminosity of the shell over the quasi-steady state (Jones et al. 2017), which implies that $v_e \propto L$, we obtain that $Ri_B \propto L^{-2/3}$. Interestingly, we find the same dependence when starting from the formula for Ri_B (given in equation A5), considering that the buoyancy jump remains constant (which is reasonable for a given initial stratification) and that $v_{rms} \propto L^{1/3}$. Using the relation $Ri_B \propto L^{-2/3}$, the boost of a factor of 1000 in the luminosity of our 3D models thus implies a reduction by a factor of 100 in Ri_B. This brings the values of the bulk Richardson number between our 3D and 1D models of the carbon shell into a reasonable agreement (see Section 4.5.6). A complication involves calculating the buoyancy jump needed for the bulk Richardson number since it is not precisely defined in a complex, stratified situation like a stellar interior – the length-scale used for this integration is therefore somewhat arbitrary.

Another important point is that we confirm with the 3D simulations that the lower boundary is stiffer than the upper boundary, by a factor of about 13 in terms of Ri_B. The fact that the entrainment velocity at the lower boundary is a factor of about 7 smaller than at the upper boundary is partly explained by the fact that the horizontal velocities at the lower boundary are higher than at the upper boundary (see Fig. 6).

Theoretical relations like the entrainment law will be needed to determine entrainment velocities for different burning stages and their various phases. This can be achieved by first estimating the bulk Richardson number of a given convective boundary from the luminosity, as described above. Then, one can approximate a turbulent rms velocity using the velocity calculated from MLT or a similar method. Finally, equation (16) can be used with suitable values for the entrainment coefficient and exponent to estimate the entrainment velocity of the mentioned convective boundary (e.g. Deardorff 1980; Fernando 1991; Stevens & Lenschow 2001; Meakin & Arnett 2007b; Chemel et al. 2010).

5 COMPARISON TO OTHER SIMULATIONS

As found by Cristini et al. (2016) using the same 1D stellar model used for these hydrodynamic simulations, the lower convective boundary is stiffer than the upper boundary as determined by the bulk Richardson number. Our higher resolution 3D models produce comparable results for the bulk Richardson number and for the `hrez` model, we obtain values of 20 and 251 for the upper and lower boundaries, respectively.

Meakin & Arnett (2007b) simulated the oxygen shell of a 23 M$_\odot$ star in spherical coordinates, also using the PROMPI code. The driving of the carbon shell we simulate is similar to their oxygen shell, owing to the fact that we boosted the luminosity. We find that the profiles of the velocity components are comparable between the two models. As shown by our Fig. 15 and their fig. 26, we find similar estimates of the bulk Richardson numbers, while the values of the constants A and n (from equation 16) differ, this is somewhat expected as the oxygen shell engulfs the neon-burning shell and complex multiple shell burning proceeds.

We obtain a TKE budget that is in agreement with that of spherical simulations of the oxygen shell in a 23 M$_\odot$ star by Viallet et al. (2013). In such an energy budget, we see a statistically steady state of turbulence over four convective turnovers. Predominantly, this is driven from the bottom of the shell by a positive rate of work due to buoyancy and dissipated at the grid scale by a numerical viscosity.

In recent full 4π simulations of the oxygen-burning shell in a 25 M$_\odot$ star, Jones et al. (2017) find a 2σ fluctuation in their calculation of the convective boundary of 17 per cent of the local pressure scaleheight. This is larger than the horizontal fluctuation in our estimation of the upper boundary of the carbon shell; a 2σ fluctuation of 4.3 per cent of the local pressure scaleheight (Fig. 13). This difference could be due to the maximum tangential velocity gradient method that Jones et al. (2017) use to estimate the boundary positions, which differs from the method described in Section 4.5.1. We find comparable magnitudes of the velocity components (see our Fig. 6, and their fig. 11), and also similar Mach numbers for the flow (see our Table 1, and their table 1). This could be in part due to the fact that our boosted energy generation rate ($\sim 3 \times 10^{12}$ erg g^{-1} s^{-1}) is comparable to the rate used in their PPMSTAR (Woodward et al. 2015) simulations. The relative magnitude of the radial velocity component in Fig. 6 is higher than that of Jones et al. (2017), and our horizontal velocity does not possess the same symmetry as their tangential velocity. The latter could be due to the difference in geometries between the two simulations. Jones et al. (2017) also observe entrainment at the upper convective boundary of their oxygen shell. Their velocity of the upper boundary due to entrainment is

lower than the entrainment velocity we estimate by over an order of magnitude. One reason for this difference could be that the oxygen shell boundary is much stiffer than the carbon shell boundary, due to a smaller jump in buoyancy over the boundary (rms turbulent velocities are similar). We determined this difference in boundary stability through the difference in the peak squared Brunt–Väisälä frequencies. The value for the upper boundary of the carbon shell (~ 0.05 rad s^{-2}) is an order of magnitude smaller than that of the oxygen shell. This could explain the order of magnitude difference in entrainment velocity assuming that the oxygen shell simulations also follow an entrainment law of the form of equation (16).

6 CONCLUSIONS

3D hydrodynamic simulations that represent the second carbon shell of a $15\,M_\odot$ star have been performed, using the PROMPI code. The initial conditions used were finely mapped profiles of the carbon shell structure from a $15\,M_\odot$, solar metallicity, non-rotating stellar model calculated by Cristini et al. (2016) using the GENEC code. The luminosity of the 3D model was provided by a parametrized nuclear energy generation rate, energy losses were also accounted for through escaping neutrinos, using a specific neutrino production rate, although their effect was negligible. The luminosity of the model was boosted by a factor of 1000 in order to ease the time needed to establish the turbulent velocity field, as discussed in Section 3.2. The computational domain utilized a plane-parallel geometry within a Cartesian coordinate system and used a parametrized gravitational acceleration.

We tested the dependence of our set-up on the domain mesh size by computing models of four different resolutions: 128^3, 256^3, 512^3, and 1024^3. At these resolutions, approximate numerical Reynolds number of 650, 1600, 4000, and 10^4, respectively are achieved in the convective zone (using equation 11). This means that with the exception of the lrez model, all of the models reach the turbulent regime (Re$_{eff} \gtrsim 1000$). While a resolution of 512^3 appears to produce a converged result at the upper boundary; the stiffer, lower boundary continues to change up to our highest resolution model. An even higher resolution run is thus planned.

We observed entrainment of material at both convective boundaries for all of the models considered. This entrainment over the quasi-steady turbulent state is associated with an almost constant velocity, and the corresponding time-scale is greater than the time-scale for the largest fluid elements to transit the convective region, asserting that convective boundary mixing in these models occurs within the equilibrium entrainment regime. The average entrainment velocities over the respective boundaries are 2.2×10^4 and -0.3×10^4 cm s^{-1} for the upper and lower boundaries, respectively. We also found that the entrainment velocity scales with the stiffness (bulk Richardson number) of the convective boundaries. This scaling follows the entrainment law with entrainment coefficient and exponent, $A = 0.03\,(\pm 0.01)$ and $n = 0.62\,(+0.09/-0.15)$, respectively. These constants were obtained from only two convective boundaries. Additional simulations using different initial conditions should help explore the parameter space of the entrainment law and whether or not the parameters we derived vary significantly from one burning stage to the other. Furthermore, the dependence on the Péclet number needs to be further explored before our results obtained in the neutrino-cooled advanced phases can be applied to the early phases (hydrogen and helium burning) during which thermal effects are important, at least at the small scales (see discussion in Viallet et al. 2015). We also estimated the boundary widths and found these to be roughly 30 per cent and 10 per cent of the local

pressure scaleheight for the upper and lower convective boundaries, respectively. While these widths are only estimates, they confirm that the lower boundary is narrower than the upper boundary.

Although more 3D simulations of all burning stages are needed to fully characterize convective boundary mixing, we can already compare our results to those of previous studies as well as the 1D input stellar model and relate them via measures of the turbulent driving and boundary stiffness. For this purpose, we investigated how entrainment and turbulent velocities, the driving luminosity and boundary stiffness (measured using the bulk Richardson number) relate to each other in Section 4.6. Considering these relations enabled us to reconcile the convective boundary properties of the carbon shell estimated from the initial 1D stellar evolution model to the properties of boundaries in the 3D simulations presented here (despite the artificial increase in luminosity for the 3D simulations). Referring to the similarities between carbon and oxygen shell simulations presented in Section 5, a coherent picture seems to emerge from all existing simulations related to the advanced burning stages in massive stars when considering the relations between the above quantities.

This is promising for the long-term goal of developing a convective boundary mixing prescription for 1D models which is applicable to all (or many) stages of the evolution of stars (and not only to the specific conditions studied in 3D simulations). The luminosity (driving convection) and the bulk Richardson number (a measure of the boundary stiffness) will be key quantities for such new prescriptions (also see Arnett et al. 2015).

The goal of 1D stellar evolution models is to capture the long-term (secular) evolution of the convective zone and of its boundaries, while 3D hydrodynamic simulations probe the short-term (dynamical) evolution. Keeping this in mind, the key points to take from this and previous 3D hydrodynamic studies for the development of new prescriptions in 1D stellar evolution codes are the following:

(i) Entrainment of the boundary and mixing across it occurs both at the top and bottom boundaries. Thus, 1D stellar evolution models should include convective boundary mixing at both boundaries. Furthermore, the boundary shape is not a discontinuity in the 3D hydrodynamic simulations but a smooth function of radius, sigmoid-like, a feature that should also be incorporated in 1D models.

(ii) At the lower boundary, which is stiffer, the entrainment is slower and the boundary width is narrower. This confirms the dependence of entrainment and mixing on the stiffness of the boundary.

(iii) Since the boundary stiffness varies both in time and with the convective boundary considered, a single constant parameter is probably not going to correctly represent the dependence of the mixing on the instantaneous convective boundary properties. As discussed above, we suggest the use of the bulk Richardson number in new prescriptions to include this dependence.

REFERENCES

Alexander D. R., Ferguson J. W., 1994, ApJ, 437, 879
Almgren A. S., Bell J. B., Zingale M., 2007, J. Phys.: Conf. Ser., 78, 012085
Angulo C. et al., 1999, Nucl. Phys. A, 656, 3
Arnett W. D., 1968, Nature, 219, 1344
Arnett D., 1994, ApJ, 427, 932
Arnett D., 1996, Supernovae and Nucleosynthesis: An Investigation of the History of Matter from the Big Bang to the Present. Princeton Univ. Press, Princeton, NJ
Arnett W. D., Meakin C., 2011a, ApJ, 733, 78
Arnett W. D., Meakin C., 2011b, ApJ, 741, 33
Arnett W. D., Meakin C., 2016, Rep. Prog. Phys., 79, 102901
Arnett W. D., Meakin C., Viallet M., 2014, AIP Adv., 4, 041010
Arnett W. D., Meakin C., Viallet M., Campbell S. W., Lattanzio J. C., Mocák M., 2015, ApJ, 809, 30
Asida S. M., Arnett D., 2000, ApJ, 545, 435
Aspden A., Nikiforakis N., Dalziel S., Bell J., 2008, Commun. Appl. Math. Comput. Sci., 3, 103
Audouze J., Chiosi C., Woosley S. E., 1986, in Audouze J., Chiosi C., Woosley S. E., eds, Saas-Fee Advanced Course 16: Nucleosynthesis and Chemical Evolution. Geneva Observatory, Sauverny
Bazan G., Arnett D., 1994, ApJ, 433, L41
Bazán G., Arnett D., 1997, Nucl. Phys. A, 621, 607
Bazán G., Arnett D., 1998, ApJ, 496, 316
Beaudet G., Petrosian V., Salpeter E. E., 1967, ApJ, 150, 979
Boldyrev S., Cattaneo F., 2004, Phys. Rev. Lett., 92, 144501
Chemel C., Staquet C., Chollet J.-P., 2010, Nonlinear Process. Geophys., 17, 187
Colella P., Woodward P. R., 1984, J. Comput. Phys., 54, 174
Couch S. M., Chatzopoulos E., Arnett W. D., Timmes F. X., 2015, ApJ, 808, L21
Cristini A., Meakin C., Hirschi R., Arnett D., Georgy C., Viallet M., 2016, Phys. Scr., 91, 034006
Damköhler G., 1940, Z. Elektrochem. Angew. Physik. Chem., 46, 601
Deardorff J. W., 1980, Bound.-Layer Meteorol., 18, 495
de Jager C., Nieuwenhuijzen H., van der Hucht K. A., 1988, A&AS, 72, 259
Denissenkov P. A., Herwig F., Bildsten L., Paxton B., 2013a, ApJ, 762, 8
Denissenkov P. A., Herwig F., Truran J. W., Paxton B., 2013b, ApJ, 772, 37
Eggenberger P., Meynet G., Maeder A., Hirschi R., Charbonnel C., Talon S., Ekström S., 2008, Ap&SS, 316, 43
Fedorovich E., Conzemius R., Mironov D., 2004, J. Atmos. Sci., 61, 281
Fernando H. J. S., 1991, Annu. Rev. Fluid Mech., 23, 455
Freytag B., Ludwig H.-G., Steffen M., 1996, A&A, 313, 497
Fryxell B., Müller E., Arnett D., 1989, in Hillebrandt W., Müller E., eds, Nuclear Astrophysics. Springer, Berlin Heidelberg, p. 100
Fryxell B. et al., 2000, ApJS, 131, 273

Garcia J., Mellado J., 2014, J. Atmos. Sci., 71, 1935
Gastine T., Wicht J., Aurnou J. M., 2015, J. Fluid Mech., 778, 721
Georgy C., Saio H., Meynet G., 2014, MNRAS, 439, L6
Gilet C., Almgren A. S., Bell J. B., Nonaka A., Woosley S. E., Zingale M., 2013, ApJ, 773, 137
Grinstein F., Margolin L., Rider W., 2007, Implicit Large Eddy Simulation – Computing Turbulent Fluid Dynamics. Cambridge Univ. Press, Cambridge
Jones S., Andrassy R., Sandalski S., Davis A., Woodward P., Herwig F., 2013, ApJ, 772, 150
Jones S., Andrassy R., Sandalski S., Davis A., Woodward P., Herwig F., 2017, MNRAS, 465, 2991
Jonker H. J. J., van Reeuwijk M., Sullivan P. P., Patton E. G., 2013, J. Fluid Mech., 732, 150
Kolmogorov A., 1941, DoSSR, 30, 301
Kolmogorov A. N., 1962, J. Fluid Mech., 13, 82
Kuhlen M., Woosley W. E., Glatzmaier G. A., 2003, in Turcotte S., Keller S. C., Cavallo R. M., eds, ASP Conf. Ser., Vol. 293, 3D Stellar Evolution. Astron. Soc. Pac., San Francisco, p. 147
Kuranz C. C. et al., 2011, Ap&SS, 336, 207
Lautrup B., 2011, Physics of Continuous Matter: Exotic and Everyday Phenomena in the Macroscopic World. CRC Press, Boca Raton, FL
Liu Y., Ecke R. E., 2011, Phys. Rev. E, 84, 016311
Lorenz E. N., 1963, J. Atmos. Sci., 20, 130
Maeder A., 2009, Physics, Formation and Evolution of Rotating Stars. Springer, Berlin Heidelberg
Maeder A., Meynet G., Lagarde N., Charbonnel C., 2013, A&A, 553, A1
Martins F., Palacios A., 2013, A&A, 560, A16
Meakin C. A., 2006, PhD thesis, University of Arizona
Meakin C. A., Arnett D., 2006, ApJ, 637, L53
Meakin C. A., Arnett D., 2007a, ApJ, 665, 690
Meakin C. A., Arnett D., 2007b, ApJ, 667, 448
Miernik J. et al., 2013, Acta Astron., 82, 173
Mocák M., Meakin C., Viallet M., Arnett D., 2014, preprint (arXiv:e-prints)
Müller B., Viallet M., Heger A., Janka H.-T., 2016, ApJ, 833, 124
Porter D. H., Woodward P. R., 2000, ApJS, 127, 159
Prialnik D., 2000, An Introduction to the Theory of Stellar Structure and Evolution. Cambridge Univ. Press, Cambridge
Rogers F. J., Swenson F. J., Iglesias C. A., 1996, ApJ, 456, 902
Schaller G., Schaerer D., Meynet G., Maeder A., 1992, A&AS, 96, 269
Schwarzschild K., Voigt H.-H., 1992, Gesammelte Werke/Collected Works. Springer, Berlin
Stevens B., Lenschow D. H., 2001, Bull. Am. Meteorol. Soc., 82, 283
Stothers R. B., Chin C.-W., 1991, ApJ, 381, L67
Sullivan P. P., Patton E. G., 2011, J. Atmos. Sci., 68, 2395
Sullivan P. P., Moeng C.-H., Stevens B., Lenschow D. H., Mayor S. D., 1998, J. Atmos. Sci., 55, 3042
Sytine I. V., Porter D. H., Woodward P. R., Hodson S. W., Winkler K.-H., 2000, J. Comput. Phys., 158, 225
Tayar J. et al., 2017, ApJ, 840, 17
Timmes F. X., Arnett D., 1999, ApJS, 125, 277
Timmes F. X., Swesty F. D., 2000, ApJS, 126, 501
Turner J. S., 1973, Buoyancy Effects in Fluids. Cambridge University Press, Cambridge
van Dyke M., 1982, NASA STI/Recon Technical Report A, 82, An Album of Fluid Motion. Parabolic Press, Stanford
van Reeuwijk M., Hunt G. R., Jonker H. J., 2011, J. Phys.: Conf. Ser., 318, 042061
Viallet M., Meakin C., Arnett D., Mocák M., 2013, ApJ, 769, 1
Viallet M., Meakin C., Prat V., Arnett D., 2015, A&A, 580, A61
Vink J. S., de Koter A., Lamers H. J. G. L. M., 2001, A&A, 369, 574
Woodward P. R., Herwig F., Lin P.-H., 2015, ApJ, 798, 49
Young P. A., Meakin C., Arnett D., Fryer C. L., 2005, ApJ, 629, L101
Zahn J.-P., 1991, A&A, 252, 179

APPENDIX A: 1D STELLAR CONVECTION PARAMETERS

To determine averages over the convective region, we used an rms mass average. The mass average of a quantity A is defined as:

$$A_{\text{avg}} = \sqrt{\frac{1}{m_2 - m_1} \int_{m_1}^{m_2} A^2(m) \, dm}, \tag{A1}$$

where m_1 and m_2 are the mass at the lower and upper convective boundaries, respectively.

The bulk Richardson number is the ratio of the boundary stabilizing potential to the kinetic energy of turbulent motions (within the convective region). It characterizes the boundary stiffness, and is a function of the Brunt–Väisälä frequency or buoyancy frequency, N, which is defined as:

$$N^2 = -g \left(\frac{\partial \ln \rho}{\partial r} \bigg|_e - \frac{\partial \ln \rho}{\partial r} \bigg|_s \right), \tag{A2}$$

where g is the gravitational acceleration, ρ is the density, and subscripts e and s represent the fluid element and its surroundings, respectively.

In order to study the properties of the boundary regions, we first need a definition of the boundary location, r_c. Meakin & Arnett (2007b) use the maximum gradient method on the composition to determine the location of convective boundaries in the oxygen shell of a $23 \, M_\odot$ model. In a similar manner, we approximate the location of the top (bottom) boundary as the vertical coordinate having an average atomic mass, $\overline{A}$, equal to the average between the convective zone and top (bottom) radiative zone,

$$\overline{A}_{\text{th}} = \frac{\overline{A}_{\text{conv}} + \overline{A}_{\text{rad}}}{2}, \tag{A3}$$

where $\overline{A}_{\text{conv}}$ and $\overline{A}_{\text{rad}}$ are the averages of $\overline{A}$ in the convective and relevant stable/radiative regions, respectively.

The buoyancy jump over a convective boundary region can be estimated by integrating the square of the buoyancy frequency over a suitable distance (Δr) either side of the boundary centre, r_c,

$$\Delta B = \int_{r_c - \Delta r}^{r_c + \Delta r} N^2 \mathrm{d}r. \tag{A4}$$

The integration distance Δr is not well-defined theoretically but it should be large enough to capture the dynamics of the boundary region and the distance over which fluid elements are decelerated.

As mentioned above, the bulk Richardson number is the ratio of the boundary stabilization potential (which includes the buoyancy jump) to the kinetic energy due to turbulent motions (within the convective region),

$$\text{Ri}_{\text{B}} = \frac{\Delta B \ell}{v_{\text{rms}}^2}, \tag{A5}$$

where ℓ is the integral length-scale which represents the size of the largest fluid elements. The integral length-scale is often taken to be the horizontal correlation length. Meakin & Arnett (2007b) show that the horizontal correlation length-scale and pressure scaleheight are similar to within a factor ~ 3. So for our analysis, we use the pressure scaleheight close to the boundary. The rms velocity, v_{rms}, represents the velocity of the largest fluid elements carrying most of the energy, which for the 1D simulations we approximate as the convective velocity,

$$v_c = \left(\frac{F_c}{\rho} \right)^{\frac{1}{3}}, \tag{A6}$$

where F_c is the convective flux.

In estimating the Mach number, we determine the sound speed, c_s, using the Helmholtz EOS (Timmes & Arnett 1999; Timmes & Swesty 2000),

$$\text{Ma} = \frac{v_c}{c_s}. \tag{A7}$$

The Péclet number (Pe) is defined as the ratio of the time-scale for advective transport to the time-scale for transport through diffusion. In the stellar case, thermal diffusion dominates over molecular diffusion. For the deep interior heat transfer plays a minor role, so typically Pe $\gg 1$. We determine the Péclet number using the following formula,

$$\text{Pe} = \frac{3 D_{\text{mlt}}}{\chi}, \tag{A8}$$

where D_{mlt} is the diffusion coefficient calculated using MLT, $D_{\text{mlt}} = v_{\text{mlt}} \ell_{\text{mlt}} / 3$, v_{mlt} and ℓ_{mlt} are the mixing length velocity and mixing length parameter. χ is the thermal diffusivity, defined as,

$$\chi = \frac{16 \sigma \, T^3}{3 \kappa \, \rho^2 \, c_p} \tag{A9}$$

where σ is the Stefan–Boltzmann constant, T the temperature, κ the Rosseland mean opacity, and c_p the specific heat capacity at constant pressure.

The Damköhler number (Da) is defined as the ratio of the advective time-scale to the nuclear reaction time-scale, generally this is small in deep convective regions as the time-scale for nuclear reactions is long, but during the advanced stages of massive star evolution the two time-scales can become comparable. We determine the Damköhler number using the following formula,

$$\text{Da} = \frac{t_{\text{con}}}{t_{\text{nuc}}} = \left(\frac{2 \ell_c}{v_c} \right) \left(\frac{q X_i}{\epsilon_{\text{nuc}}} \right)^{-1}, \tag{A10}$$

where t_{con} is the convective turnover time and t_{nuc} is the relevant nuclear reaction time-scale. ℓ_c is the height of the convective zone, q is the specific energy released for the dominating reactions, X_i is the mass abundance of the interacting particles, and ϵ_{nuc} is the nuclear energy generation rate.

The majority of these variables are presented in Table A1 for most of the convective boundaries shown in Fig. 1.

Table A1. Estimates of the convective velocity ($cm\,s^{-1}$), Bulk Richardson number, Mach number, Péclet number, and Damköhler number of different times during core- and shell-burning phases of a $15\,M_\odot$ stellar model. Bulk Richardson numbers are boundary values, brackets indicate values at the lower boundary, all other values were mass averaged over the convective region. Péclet numbers are order of magnitude estimates.

Phase	v_c ($cm\,s^{-1}$)	Ri_B	Ma	Pe	Da
H Core Start	6.9×10^4	1.8×10^2	9.3×10^{-4}	$\sim 10^3$	3.8×10^{-8}
H Core End	9.7×10^4	1.1×10^2	1.5×10^{-3}	$\sim 10^3$	7.2×10^{-7}
He Core Start	4.7×10^4	1.2×10^3	4.3×10^{-4}	$\sim 10^4$	1.8×10^{-7}
He Core Max	5.9×10^4	4.0×10^2	5.0×10^{-4}	$\sim 10^5$	3.5×10^{-6}
He Core End	5.9×10^4	3.8×10^2	5.1×10^{-4}	$\sim 10^5$	3.0×10^{-6}
C Core Start	6.9×10^4	7.2×10^3	3.0×10^{-4}	$\sim 10^6$	3.4×10^{-6}
C Core Max	5.6×10^4	1.2×10^4	2.4×10^{-4}	$\sim 10^7$	1.2×10^{-5}
C Core End	5.8×10^4	3.9×10^2	2.4×10^{-4}	$\sim 10^7$	1.8×10^{-5}
Ne Core Start	1.5×10^6	82	3.9×10^{-3}	$\sim 10^{10}$	3.3×10^{-3}
Ne Core Max	6.4×10^5	3.6×10^2	1.9×10^{-3}	$\sim 10^{10}$	5.5×10^{-3}
Ne Core End	4.1×10^5	62	1.1×10^{-3}	$\sim 10^{10}$	2.6×10^{-3}
O Core Start	8.8×10^5	2.4×10^2	2.2×10^{-3}	$\sim 10^{10}$	6.3×10^{-4}
O Core Max	7.9×10^5	8.5×10^4	2.0×10^{-3}	$\sim 10^{10}$	2.4×10^{-3}
O Core End	7.5×10^5	27	1.8×10^{-3}	$\sim 10^{10}$	2.0×10^{-3}
He Shell Start	1.4×10^5	46(20)	8.9×10^{-4}	$\sim 10^6$	5.7×10^{-8}
He Shell End	1.3×10^5	$14(1.8 \times 10^3)$	9.1×10^{-4}	$\sim 10^6$	1.0×10^{-7}
C Shell Start	3.6×10^5	$4.2 \times 10^2(6.0 \times 10^3)$	1.3×10^{-3}	$\sim 10^8$	1.3×10^{-4}
C Shell IC^a	2.9×10^5	$6.9 \times 10^2(1.5 \times 10^4)$	1.2×10^{-3}	$\sim 10^8$	2.0×10^{-4}
C Shell End	1.6×10^5	$59(6.5 \times 10^4)$	5.7×10^{-4}	$\sim 10^7$	1.3×10^{-4}
O Shell Start	1.5×10^5	$3.7 \times 10^4(4.0 \times 10^4)$	3.4×10^{-4}	$\sim 10^{10}$	2.7×10^{-4}
O Shell End	5.7×10^5	$1.2 \times 10^2(3.4 \times 10^4)$	1.3×10^{-3}	$\sim 10^{10}$	1.4×10^{-3}

^{a} Properties of the 1D model used as initial conditions for the 3D simulations.

Table A2. Constants used in the fitting functions (equation B1) for the five sections of the entropy, $\bar{A}$ and $\bar{Z}$ profiles. Subscripts 1,2, and 3 refer to the lower stable, convective, and upper stable sections, respectively. Subscripts l and u refer to the lower and upper convective boundary sections, respectively.

	α_1	β_1	θ_1	ϕ_1	η_1	α_2	β_2	θ_u	ϕ_u	η_u	α_3	β_3
s	1.65×10^8	0.24	2.81×10^8	3.43×10^8	-0.5	3.43×10^8	0	3.43×10^8	3.56×10^8	-0.5	3.56×10^8	0.08
$\bar{A}$	18.17	0	18.17	16.19	0.5	16.19	0	16.19	14.38	0.5	14.38	0
$\bar{Z}$	9.07	0	9.07	8.08	0.5	8.08	0	8.08	7.18	0.5	7.18	0

APPENDIX B: STELLAR MODEL PROFILE FITTING

The entropy (s), average atomic mass ($\bar{A}$), and average atomic number ($\bar{Z}$) were remapped by considering five distinct sections of the domain. The lower stable region (below the lower convective boundary), the convective region, and the upper stable region (above the upper boundary) were fitted linearly in the form $\alpha + \beta x$, where α and β are constants, and x is the radius on a grid point. The two remaining sections are the upper and lower convective boundaries, these were fitted using sigmoid functions, f_{sig}, of the form,

$$f_{sig} = \theta + \frac{\phi - \theta}{1 + e^{\eta z}}, \tag{B1}$$

where θ, ϕ, and η are constants, and z is a normalized grid index. The fitting constants for the three variables are presented in Table A2, the subscripts for each constant represent the section of the domain for which the fit refers to. Subscripts 1, 2, and 3 denote the lower stable, convective, and upper stable sections, respectively. Subscripts l and u refer to the lower and upper convective boundary sections, respectively.

APPENDIX C: RANS TERMINOLOGY AND THE TURBULENT KINETIC ENERGY EQUATION

In the RANS framework, variables are split into mean and fluctuating components. The horizontally averaged mean is denoted by angled brackets and defined as,

$$\langle a \rangle = \frac{1}{\Delta A} \int_{\Delta A} a \, dA, \tag{C1}$$

where $dA = dy\,dz$ and $\Delta A = \Delta y \Delta z$ is the area of the computational domain. The fluctuating component, a', is obtained by subtracting the mean of the variable from the variable: $a' = a - \langle a \rangle$.

In order to statistically sample, the quasi-steady state we perform temporal averaging over several convective turnovers, denoted by an overbar and defined as,

$$\bar{a} = \frac{1}{\Delta t} \int_{t_1}^{t_2} a(t) \, dt, \tag{C2}$$

for an averaging window $\Delta t = t_2 - t_1$.

The Eulerian equation of TKE can be written as (equation A12 of Meakin & Arnett 2007b):

$$\partial_t (\rho E_k) + \nabla \cdot (\rho E_k \boldsymbol{v}) = -\boldsymbol{v} \cdot \nabla p + \rho \, \boldsymbol{v} \cdot \boldsymbol{g} \tag{C3}$$

where $\boldsymbol{v}$ is the velocity and $E_k = \frac{1}{2}(\boldsymbol{v} \cdot \boldsymbol{v})$ is the specific kinetic energy.

Applying horizontal and temporal averaging to equation (C3) yields the mean TKE equation, which can be written as,

$$\overline{\langle \rho \mathbf{D_t} E_k \rangle} = -\nabla \cdot \overline{\langle \mathbf{F_p} + \mathbf{F_k} \rangle}$$
$$+ \overline{\langle \mathbf{W_p} \rangle} + \overline{\langle \mathbf{W_b} \rangle} - \epsilon_k, \tag{C4}$$

where $\mathbf{D_t} = \partial_t + \nabla \cdot \boldsymbol{v}$ is the material derivative,

$\mathbf{F_p} = p' \boldsymbol{v}'$ is the turbulent pressure flux,
$\mathbf{F_k} = \rho E_k \boldsymbol{v}'$ is the TKE flux,
$\mathbf{W_p} = p' \nabla \cdot \boldsymbol{v}'$ is the pressure dilatation,
$\mathbf{W_b} = \rho' \boldsymbol{g} \cdot \boldsymbol{v}'$ is the work due to buoyancy and
ϵ_k is the numerical dissipation of kinetic energy.

This paper has been typeset from a TEX/LATEX file prepared by the author.